

Variational Inference for Deblending Crowded Starfields

Runjing Liu ^{*}

Department of Statistics, University of California, Berkeley

Jon D. McAuliffe

The Voleon Group

Department of Statistics, University of California, Berkeley

Jeffrey Regier

Department of Statistics, University of Michigan

The LSST Dark Energy Science Collaboration

Abstract

In the image data collected by astronomical surveys, stars and galaxies often overlap. Deblending is the task of distinguishing and characterizing individual light sources from survey images. We propose StarNet, a fully Bayesian method to deblend sources in astronomical images of crowded star fields. StarNet leverages recent advances in variational inference, including amortized variational distributions and the wake-sleep algorithm. Wake-sleep, which minimizes forward KL divergence, has significant benefits compared to traditional variational inference, which minimizes a reverse KL divergence. In our experiments with SDSS images of the M2 globular cluster, StarNet is substantially more accurate than two competing methods: Probabilistic Cataloging (PCAT), a method that uses MCMC for inference, and a software pipeline employed by SDSS for deblending (DAOPHOT). In addition, StarNet is as much as 100,000 times faster than PCAT, exhibiting the scaling characteristics necessary to perform fully Bayesian inference on modern astronomical surveys.

Keywords: Bayesian methods, amortized inference, wake-sleep algorithm, approximate inference, astronomical surveys, cataloging.

^{*}Runjing Liu (e-mail: runjing_liu@berkeley.edu) gratefully acknowledges support from the NSF Graduate Research Fellowship Program. This paper has been approved by the LSST Dark Energy Science Collaboration following an internal review. The internal reviewers were Bastien Arcelin, François Lanusse, and Peter Melchior. The authors also thank Derek Hansen, Ismael Mendoza, and Zhe Zhao for reviewing this manuscript and for continuing the development of our software.

1 Introduction

Astronomical images record the arrival of photons from distant light sources. Astronomical catalogs are constructed from these images. Catalogs label light sources as stars, galaxies, or other objects; they also list the physical characteristics of light sources such as flux, color, and morphology. These catalogs are the starting point for many downstream analyses. For example, Bayestar used a catalog of stellar fluxes and colors to construct the 3D distribution of interstellar dust (Green et al., 2019). Catalogs of galaxy morphologies have been used to validate theoretical models of dark matter and dark energy (Abbott et al., 2018).

A light source, be it a star or a galaxy, produces a peak intensity of brightness in an image. When light sources are well separated, catalog construction is straightforward: characteristics of each light source, such as flux, can be estimated by analyzing intensities at the peak and surrounding pixels. However, in images crowded with many light sources, observed intensities may result from the combined light of multiple sources. Source separation, or *deblending*, is the task of differentiating and characterizing individual light sources from a mixture of intensities on an image. A key challenge in deblending is inferring whether an observed intensity is in fact blended, that is, whether it is composed of a single bright source or multiple dimmer sources.

Deblending is challenging for several reasons. First, it is an unsupervised problem without ground truth labeled data. Second, it is a problem with a sample size of one: there is only one night sky, which is imaged many times, and the collected survey images capture overlapping regions of it. Third, for blended fields, the properties of light sources are ambiguous; therefore, providing calibrated uncertainties for catalog construction is as important as making accurate predictions. Finally, the scale of the data is immense. The upcoming Rubin Observatory Legacy Survey of Space and Time (LSST), scheduled to begin data collection in 2022, is expected to produce 60 petabytes of astronomical images over its lifetime (LSST, 2020).

As more powerful telescopes are developed, and their ability to detect more distant light sources improves, the density of light sources in the images they capture will only increase. For instance, Bosch et al. (2018) estimates that 58% of light sources are blended in images captured by the Subaru Telescope’s Hyper Suprime-Cam, and that percentage is expected to increase for LSST. Therefore, developing a method that reliably characterizes light sources, even in cases of significant light source blending, advances any astronomical research in which conclusions about the physical universe are derived from estimated catalogs.

We focus on cataloging applications where all light sources are well modeled as points without spatial extent. Point-source-only models are applicable to surveys such as DE-Cam (Schlafly et al., 2018), which imaged the center of the Milky Way, and WISE (Wright et al., 2010), whose telescope resolution did not allow for differentiation between stars and

galaxies. In this work, we use the globular cluster M2, a region imaged by the Sloan Digital Sky Survey (SDSS) that is densely populated with stars, as a test bed for our method.

From software pipelines to probabilistic cataloging

Traditionally, most cataloging has been performed using software pipelines. These pipelines are algorithms that usually involve the following stages: locating the brightest peaks, estimating fluxes, and subtracting the estimated light source. These stages may be performed iteratively. Pipelines do not normally produce statistically calibrated error estimates that propagate the uncertainty that accumulates in each of the steps. Failure to properly accumulate error at each step results in unreliable catalogs for images in which ambiguity exists in identifying sources and estimating their characteristics. For example, PHOTO (Lupton et al., 2001), the default cataloging pipeline used by the Sloan Digital Sky Survey (SDSS), failed to produce a catalog on the globular cluster M2 (Portillo et al., 2017).

In contrast, *probabilistic* cataloging posits a statistical model consisting of a likelihood for the observed image given a catalog and a prior distribution over possible catalogs (Portillo et al., 2017; Brewer et al., 2013; Feder et al., 2020). Instead of deriving a single catalog, probabilistic cataloging produces a posterior distribution over the set of all possible catalogs. Uncertainties are quantified by the posterior distribution. For example, in an image with an ambiguously blended bright peak, some catalogs sampled from the posterior would contain multiple dim light sources while others would contain one bright source. The relative density the posterior distribution places on one explanation over another represents the statistical confidence in that explanation. Moreover, a distribution over the set of all catalogs induces a distribution on any estimate derived from a catalog. Therefore, calibrated uncertainties can be propagated to downstream analyses.

Previous work on probabilistic cataloging employed Markov chain Monte Carlo (MCMC) to sample from the posterior distribution. The MCMC procedure in Portillo et al. (2017) and Feder et al. (2020) was called PCAT, short for “Probabilistic CATaloging.”¹ Because the posterior is defined over the set of all catalogs and the number of sources in a catalog is unknown and random, the latent variable space is transdimensional. PCAT used reversible jump MCMC (Green, 1995) to sample transdimensional catalogs. In reversible jump MCMC, auxiliary variables are added to encode the “birth” of new light sources or the “death” of existing ones in the Markov chain.

The computational cost of MCMC for this model is problematic for large-scale astronomical surveys. Early implementations of PCAT required a day to process a 100×100 pixel image of the M2 globular cluster imaged by SDSS (Portillo et al., 2017). More recent implementations running inexact MCMC brought the runtime down to 30 minutes (Feder

¹We use “probabilistic cataloging” to refer to any method that produces a posterior over possible catalogs, whereas “PCAT” refers specifically to the MCMC procedure in Portillo et al. (2017) and Feder et al. (2020).

et al., 2020). In any case, a 100×100 pixel image covers only a 0.66×0.66 arcminute patch of the sky. For comparison, in one night, SDSS scans a region on the order of 100×1000 arcminutes. Extrapolating the 30-minute runtime, PCAT would take about three months to process a nightly SDSS run.

As an alternative to MCMC, Regier et al. (2019) produced an approximate posterior using variational inference. Variational inference (VI) considers a family of candidate approximate posteriors and employs numerical optimization to find the distribution in the family closest in KL divergence to the exact posterior (Jordan et al., 1999; Wainwright and Jordan, 2008; Blei et al., 2017). With a sufficiently constrained family of distributions, the VI optimization problem can be solved orders of magnitude faster than MCMC runs.

However, Regier et al. (2019) is limited in that the number of light sources in a given image is treated as known and fixed – it had to be set using a preprocessing routine. This simplification was made in order to have a tractable objective for numerical optimization.

Our contribution

We propose *StarNet*, a approach to deblending that employs several recent VI innovations (Zhang et al., 2019; Le et al., 2020). Unlike Regier et al. (2019), our VI approach is able to handle arbitrary probabilistic models, including a transdimensional model with an unknown number of sources. Section 2 introduces the statistical model, which is similar to the model used in PCAT.

Secondly, again unlike Regier et al. (2019), we employ *amortization*, which enables StarNet to scale inference to large astronomical surveys. In amortized variational inference, a neural network maps input images to an approximate posterior. Following a one-time cost to fit the neural network, inference on new images requires just a single forward pass. Rapid inference is available without the need to re-run MCMC or numerically optimize VI for each new image. For StarNet, the forward pass on a 100×100 pixel image takes 0.2 seconds (vs. 30 minutes for inference using PCAT). Section 3 details the variational distribution and neural network architecture in StarNet.

Finally, and critically, StarNet is fit using the wake-sleep algorithm (Hinton et al., 1995), which does not target the same KL divergence traditionally used in variational inference. Traditionally, variational inference minimizes the “reverse” KL divergence between the approximate posterior q and the exact posterior p . Reverse KL is defined as the q -weighted average difference between $\log q$ and $\log p$. Wake-sleep instead fits the approximate posterior using the “forward” KL divergence, which weights the difference between $\log p$ and $\log q$ by p . The forward KL is minimized using stochastic gradient descent (SGD). At each iteration, catalogs are sampled from the prior distribution, then used to generate images from the likelihood model. The neural network is fit to map the generated images to distributions that place probability mass on their corresponding catalogs. Section 4 details the wake-sleep procedure.

In this application, optimizing the forward KL produces more reliable approximate

postiors than optimizing the traditional reverse KL (Section 5). In particular, by taking advantage of complete data—the sampled images and their corresponding catalogs—wake-sleep avoids shallow local minima where the approximate posterior returned by the neural network is far from the exact posterior in terms of KL divergence.

The wake-sleep algorithm has been used in previous research to train deep generative models (Hinton et al., 1995; Bornschein and Bengio, 2014; Le et al., 2020). However, to the best of our knowledge, this is the first application of wake-sleep for scientific purposes. Specifically, we use wake-sleep for inference to find a latent space that is interpretable: it is the set of all possible astronomical catalogs.

We applied StarNet to the M2 globular cluster as imaged by SDSS. We used the M2 catalog from the ACS Globular Cluster Survey (Sarajedini et al., 2007) as ground truth. The ACS survey used the Hubble Space telescope, which has approximately 20 times the angular resolution and 30 times the exposure of the ground-based Sloan telescope. StarNet was more accurate than the MCMC-based cataloger PCAT and traditional cataloging approaches while running 100,000 times faster than the former (Section 6). Although the MCMC posterior approximation converges to the exact posterior asymptotically, over finite horizons an MCMC sampler may not mix well. The sleep-phase objective from the Wake-Sleep algorithm allows StarNet to circumvent many of the challenges of non-convex optimization (Section 7). Code to reproduce our results is publicly available at <https://github.com/Runjing-Liu120/DeblendingStarfields>.

2 The generative model

In crowded starfields, such as globular clusters and the Milky Way, the vast majority of light sources are stars. An astronomical image records the number of photons that reached a telescope and arrived at each pixel. Typically, photons must pass through one of several filters, each selecting photons from a specified band of wavelengths, before being recorded.

For a given $H \times W$ pixel image with B filter bands, our goal is to infer a catalog of stars. The catalog specifies the number of stars in an image; for each such star, the catalog records its location and its flux, or brightness, in each band. The space of latent variables \mathcal{Z} is the collection of all possible catalogs of the form

$$z := \{N, (\ell_i, f_{i,1}, \dots, f_{i,B})_{i=1}^N\}, \quad (1)$$

where the number of stars in the catalog is $N \in \mathbb{N}$, the location of the i th star is $\ell_i \in \mathbb{R}^2$, and the flux of the i th star in the b th band is $f_{i,b} \in \mathbb{R}^+$.

A Bayesian approach requires specification of a prior over catalog space \mathcal{Z} and a likelihood for the observed images. Our likelihood and prior, detailed below, are similar to previous approaches (Brewer et al., 2013; Portillo et al., 2017; Regier et al., 2019; Feder et al., 2020).

2.1 The prior

The prior over \mathcal{Z} is a marked spatial Poisson process. To sample the prior, first draw the number of stars contained in the $H \times W$ image as

$$N \sim \text{Poisson}(\mu HW), \quad (2)$$

where μ is a hyperparameter specifying the average number of sources per pixel. Next, draw locations

$$\ell_1, \dots, \ell_N | N \stackrel{iid}{\sim} \text{Uniform}([0, H] \times [0, W]). \quad (3)$$

The fluxes in the first band are from a power law distribution with slope α :

$$f_{1,1}, \dots, f_{N,1} | N \stackrel{iid}{\sim} \text{Pareto}(f_{min}, \alpha). \quad (4)$$

Fluxes in other bands are described relative to the first band. Like Feder et al. (2020), we define the log-ratio of flux relative to the first band as “color.” Colors are drawn from a Gaussian distribution

$$c_{1,b}, \dots, c_{N,b} | N \stackrel{iid}{\sim} \mathcal{N}(\mu_c, \sigma_c^2), \quad b = 2, \dots, B. \quad (5)$$

Given the flux in the first band $f_{i,1}$ and color $c_{i,b}$, the flux in band b is $f_{i,b} = f_{i,1} \times 10^{c_{i,b}/2.5}$.

Also like Feder et al. (2020), we set the power law slope $\alpha = 0.5$ and use a standard Gaussian for the color prior ($\mu_c = 0$, $\sigma_c^2 = 1$). Appendix C evaluates the sensitivity of the resulting catalog to choices of the prior parameters.

2.2 The likelihood

Let x_{hw}^b denote the observed number of photoelectrons at pixel (h, w) in band b . For each band, at every pixel, the expected number of photoelectron arrivals is $\lambda_{hw}^b(z)$, a deterministic function of the catalog z . Motivated by the Poissonian nature of photon arrivals and the large photon arrival rate in SDSS and LSST images, observations are drawn as

$$x_{hw}^b | z \stackrel{ind}{\sim} \mathcal{N}(\lambda_{hw}^b, \lambda_{hw}^b), \quad b = 1, \dots, B; \quad h = 1, \dots, H; \quad w = 1, \dots, W, \quad (6)$$

where

$$\lambda_{hw}^b = I^b(h, w) + \sum_{i=1}^N f_{i,b} \mathcal{P}^b(h - \ell_{i,1}, w - \ell_{i,2}). \quad (7)$$

Here, \mathcal{P}^b is the point spread function (PSF) for band b and I^b is the background intensity. The PSF is a function

$$\mathcal{P}^b : \mathbb{R} \times \mathbb{R} \mapsto \mathbb{R}^+, \quad (8)$$

describing the appearance of a stellar point source at any 2D position of the image (but ignoring pixelation). Our PSF model is a weighted average between a Gaussian “core” and a power-law “wing,” as described in Xin et al. (2018). For each band, the PSF has the form

$$\mathcal{P}(u, v) = \frac{\exp\left(\frac{-(u^2+v^2)}{2\sigma_1^2}\right) + \zeta \exp\left(\frac{-(u^2+v^2)}{2\sigma_2^2}\right) + \rho(1 + \frac{v^2+u^2}{\gamma\sigma_P^2})^{-\gamma/2}}{1 + \zeta + \rho}. \quad (9)$$

The PSF parameters vary by band. Let the collection of PSF parameters across all bands be denoted $\pi := (\sigma_1^{(b)}, \sigma_2^{(b)}, \sigma_P^{(b)}, \gamma^{(b)}, \zeta^{(b)}, \rho^{(b)})_{b=1}^B$.

The background intensity at pixel (h, w) is modeled with an affine function:

$$I^b(h, w) = \beta_0^b + \beta_1^b \times h + \beta_2^b \times w. \quad (10)$$

The background parameters are specific to the band.

StarNet estimates these parameters jointly with the approximate posterior (Section 4). Prior work on probabilistic cataloging relied on estimates from the SDSS software pipeline and found the PSF estimates to be suboptimal in crowded starfields (Feder et al., 2020).

3 Variational inference

The central quantity in Bayesian statistics is the posterior distribution $p(z|x)$. However, in many nontrivial probabilistic models, including our own, the posterior distribution is intractable to calculate. Calculation of the posterior requires us to compute the marginal likelihood, $p(x)$, which involves integrating over the latent variable z . In our model, the latent variable space is high dimensional: it is the set of all catalogs. Approximate methods such as MCMC and variational inference are therefore required.

Variational inference (Jordan et al., 1999; Wainwright and Jordan, 2008; Blei et al., 2017) posits a family of distributions \mathcal{Q} and seeks the distribution $q^* \in \mathcal{Q}$ that is closest to the exact posterior in KL divergence. \mathcal{Q} is chosen such that q^* will not be too difficult to find via optimization. We index the distributions in \mathcal{Q} using a real-valued vector η , then seek η^* satisfying

$$\eta^* = \arg \min_{\eta} \text{KL}\left[q_{\eta}(z|x) \parallel p(z|x) \right]. \quad (11)$$

Minimizing the KL divergence in (11) is equivalent to maximizing the evidence lower bound (ELBO) (Blei et al., 2017):

$$\mathcal{L}_{\text{elbo}}(\eta) = \mathbb{E}_{q_{\eta}(z|x)} \left[\log p(x, z) - \log q_{\eta}(z|x) \right]. \quad (12)$$

Computing the ELBO does not require computing the marginal distribution $p(x)$, which is intractable, or the posterior distribution $p(z|x)$, which would be circular.

3.1 The variational distribution

Traditionally in variational inference, the posterior approximation q_η depends on the data x only implicitly, in that η^* is chosen according to (11). In this case, $q_\eta(z|x)$ is usually written $q_\eta(z)$, suppressing the dependence on x .

The generative model in Section 2 does not assume any hierarchical structure over replicated images. Therefore, given a new image x^{new} , the posterior factorizes; in other words, $p(z^{new}, z|x^{new}, x) = p(z^{new}|x^{new})p(z|x)$. To find a variational approximation to the posterior $p(z^{new}|x^{new})$, the optimization problem (11) must be solved again with $x = x^{new}$. Even in models with hierarchical structure, the variational distribution will generally need to be updated via optimization for every newly observed data point.

On the other hand, in *amortized* variational inference (Kingma and Welling, 2013; Rezende et al., 2014), q_η explicitly depends on the data. A flexible, parameterized function maps input x , in this case an observed image, to the parameters of a variational distribution on the latent space \mathcal{Z} . Typically, the function is a neural network, in which case the variational parameters η are the neural network weights. After the neural network is fitted with (11) using a collection of observed x 's, the approximate posterior $q_\eta(z^{new}|x^{new})$ for a new data point x^{new} can be evaluated with a single forward pass through the neural network. No additional run of an iterative optimization routine is needed for a new data point x^{new} .

The following subsections detail the construction of our variational distribution.

3.1.1 The factorization

To make the objective in (11) tractable, the family \mathcal{Q} is normally restricted to probability distributions without conditional dependencies between some latent variables. In the most extreme case, known as mean-field variational inference, the variational distribution completely factorizes across all latent variables.

Our factorization instead has a spatial structure. First, we partition the full $H \times W$ image into disjoint $R \times R$ tiles. R will be chosen such that the probability of having three or more stars in one tile is small. In this way, the cataloging problem decomposes to inferring only a few stars at a time (Section 3.1.3).

Let $S = \frac{H}{R}$ and $T = \frac{W}{R}$ and assume without loss of generality that H and W are multiples of R . For $s = 1, \dots, S$ and $t = 1, \dots, T$, the tile \tilde{x}_{st} is composed of the following pixels:

$$\tilde{x}_{st} = \{x_{hw} : Rs \leq h \leq R(s+1) \text{ and } Rt \leq w \leq R(t+1)\}. \quad (13)$$

Figure 1 gives an example with $R = 2$.

Let $\tilde{N}^{(s,t)}$ be the number of stars in tile (s, t) . Because $\tilde{N}^{(s,t)}$ is random, the cardinality of the set of locations and fluxes in each tile is also random. To handle the trans-dimensional

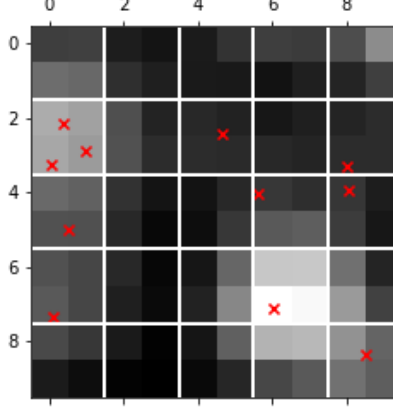


Figure 1: Tiling a 10×10 pixel image into 2×2 tiles.

parameter space, we consider a *triangular array* of latent variables on each tile:

$$\tilde{\ell}^{(s,t)} = (\tilde{\ell}_{N,i}^{(s,t)} : i = 1, \dots, N; N = 1, 2, \dots); \quad (14)$$

$$\tilde{f}^{(s,t)} = (\tilde{f}_{N,i}^{(s,t)} : i = 1, \dots, N; N = 1, 2, \dots), \quad (15)$$

where $\tilde{\ell}_{N,i}^{(s,t)}$ and $\tilde{f}_{N,i}^{(s,t)}$ are the elements of the triangular array corresponding to location and fluxes, respectively.

Tile locations $\tilde{\ell}_{N,i}^{(s,t)} \in [0, R] \times [0, R]$ give the location of stars within a tile. The fluxes $\tilde{f}_{N,i}^{(s,t)}$ are vectors in \mathbb{R}_+^B (one flux for each band).

Call $(\tilde{N}^{(s,t)}, \tilde{\ell}^{(s,t)}, \tilde{f}^{(s,t)})_{s=1, t=1}^{S, T}$ the *tile latent variables*; succinctly denote tile latent variables as \tilde{z} . The ultimate latent variable of interest is $z = \{N, (\ell_i, f_{i,1}, \dots, f_{i,B})_{i=1}^N\}$, the catalog for the full image. A distribution on z is obtained by first constructing a mapping from \tilde{z} to z . We then define a distribution on the tile latent variables \tilde{z} , which in turn induces a distribution on z .

We now detail the mapping $\tilde{z} \mapsto z$ (see Figure 2 for a schematic). The number of stars in the catalog is

$$N = \sum_{s=1}^S \sum_{t=1}^T \tilde{N}^{(s,t)}. \quad (16)$$

For every tile (s, t) , we index into the $\tilde{N}^{(s,t)}$ -th row of the triangular array of tile latent variables: the fluxes in the catalog are

$$\{f_i\}_{i=1}^N = \left\{ \tilde{f}_{\tilde{N}^{(s,t)}, i}^{(s,t)} : i = 1, \dots, \tilde{N}^{(s,t)}, s = 1, \dots, S, t = 1, \dots, T \right\}, \quad (17)$$

and the corresponding locations are

$$\{\ell_i\}_{i=1}^N = \left\{ \tilde{\ell}_{N^{(s,t)},i}^{(s,t)} + \begin{pmatrix} Rs \\ Rt \end{pmatrix} : i = 1, \dots, N^{(s,t)}, s = 1, \dots, S, t = 1, \dots, T \right\}. \quad (18)$$

The tile location is shifted by (Rs, Rt) to obtain the location in the full image.

Given this mapping from tile latent variables to the catalog of interest,

$$(\tilde{N}^{(s,t)}, \tilde{\ell}^{(s,t)}, \tilde{f}^{(s,t)})_{s=1,t=1}^{S,T} \mapsto \{N, (\ell_i, f_{i,1}, \dots, f_{i,B})_{i=1}^N\}, \quad (19)$$

a distribution on the tile latent variables induces a distribution on catalogs.

Our variational distribution on \tilde{z} factorizes over image tiles:

$$\tilde{q}_\eta((\tilde{N}^{(s,t)}, \tilde{\ell}^{(s,t)}, \tilde{f}^{(s,t)})_{s=1,t=1}^{S,T} | x) = \prod_{s=1}^S \prod_{t=1}^T \tilde{q}_\eta(\tilde{N}^{(s,t)}, \tilde{\ell}^{(s,t)}, \tilde{f}^{(s,t)} | x). \quad (20)$$

Within each tile (s, t) , the distribution also fully factorizes:

$$\tilde{q}_\eta(\tilde{N}^{(s,t)}, \tilde{\ell}^{(s,t)}, \tilde{f}^{(s,t)} | x) = \tilde{q}_\eta(\tilde{N}^{(s,t)} | x) \prod_{n=1}^{\infty} \prod_{i=1}^n \tilde{q}_\eta(\tilde{\ell}_{n,i}^{(s,t)} | x) \tilde{q}_\eta(\tilde{f}_{n,i}^{(s,t)} | x). \quad (21)$$

If τ is the mapping in (19), then the variational distribution on catalogs z is

$$q_\eta(z | x) := \tilde{q}_\eta(\tau^{-1}(z) | x), \quad (22)$$

where $\tau^{-1}(z)$ is the pre-image of z under τ .

Evaluating the variational distribution

Evaluating the ELBO requires computing the probability of $q_\eta(z | x)$ for any given catalog $z = \{N, (\ell_i, f_{i,1}, \dots, f_{i,B})_{i=1}^N\}$. By (22), it suffices to evaluate $\tilde{q}_\eta(\tau^{-1}(z) | x)$.

Here, $\tau^{-1}(z)$ is a set of tile latent variables because the mapping from tile latent variables to catalogs z is not injective, as we now explain.

Locations in the catalog $\{\ell_i\}_{i=1}^N$ determine the number of stars on tile (s, t) . The number of stars $\tilde{N}^{(s,t)}$ is simply the count of the locations that reside within that tile:

$$\tilde{N}^{(s,t)} = \sum_{i=1}^N \mathbf{1}\left\{\ell_i \in [Rs, R(s+1)] \times [Rt, R(t+1)]\right\}, \quad (23)$$

where $\mathbf{1}\{\cdot\}$ is the indicator function, equal to one if true and zero if false.

Now, consider $\tilde{\ell}^{(s,t)}$ and $\tilde{f}^{(s,t)}$, the triangular array of locations and fluxes on tile (s, t) . For each (s, t) , the $\tilde{N}^{(s,t)}$ -th row of the triangular array of fluxes and locations is determined by the locations and fluxes of stars imaged in tile (s, t) ; they are determined by the catalog z . However, the other rows of the triangular arrays are not determined by the catalog z ; they are free to take any value in their domain. Therefore, the mapping τ is not injective.

Tile latent variables

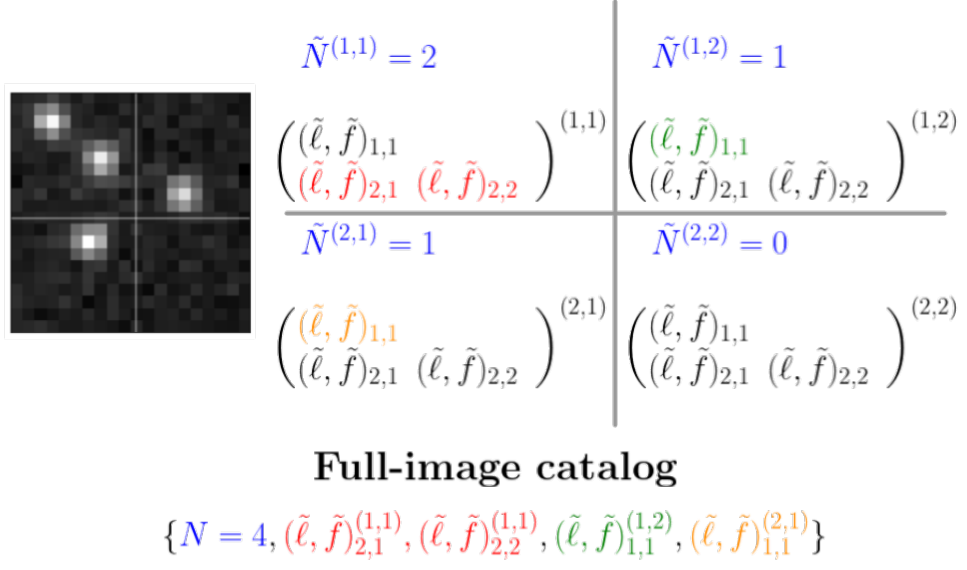


Figure 2: An example image with four tiles illustrating the relationship between tile latent variables and the full-image latent variables. The upper-left tile has two stars; the upper-right and lower-left have one; the bottom right has none. To construct the full-image catalog, we index into the appropriate row of the triangular array on each tile.

Thus, evaluating the probability of $\tau^{-1}(z)$ under \tilde{q}_η requires marginalizing over the rows of the triangular arrays $\ell^{(s,t)}$ and $\tilde{f}^{(s,t)}$ that are not determined by z . However, because \tilde{q}_η fully factorizes, the terms in (21) where $n \neq \tilde{N}^{(s,t)}$ do not enter the product after marginalization. Applying this observation and combining (21) and (20), $\tilde{q}(\tau^{-1}(z)|x)$ becomes

$$\tilde{q}(\tau^{-1}(z)|x) = \prod_{s=1}^S \prod_{t=1}^T \left\{ \tilde{q}_\eta(\tilde{N}^{(s,t)}|x) \prod_{i=1}^{\tilde{N}^{(s,t)}} \tilde{q}_\eta(\tilde{\ell}_{\tilde{N}^{(s,t)},i}^{(s,t)}|x) \tilde{q}_\eta(\tilde{f}_{\tilde{N}^{(s,t)},i}^{(s,t)}|x) \right\}. \quad (24)$$

In words, given a catalog z , first convert z to tile random variables; to compute $q_\eta(z|x)$, it suffices to evaluate \tilde{q}_η only at the rows of triangular arrays determined by the number of stars falling in each tile.

3.1.2 Variational distributions on image tiles

We describe the variational distribution on each tile, $\tilde{q}_\eta(\tilde{N}^{(s,t)}, \tilde{\ell}^{(s,t)}, \tilde{f}^{(s,t)}|x)$. Dropping the index (s, t) in this subsection,

$$\tilde{N} \sim \text{Categorical}(\omega; 0, \dots, N_{max}); \quad (25)$$

$$\tilde{\ell}_{\tilde{N},i}/R \sim \text{LogitNormal}(\mu_{\ell_{\tilde{N},i}}, \text{diag}(\nu_{\ell_{\tilde{N},i}})); \quad (26)$$

$$\tilde{f}_{\tilde{N},i}^b \sim \text{LogNormal}(\mu_{f_{\tilde{N},i}^b}, \sigma_{f_{\tilde{N},i}^b}^2), \quad (27)$$

for $i = 1, \dots, \tilde{N}$; $\tilde{N} = 1, \dots, N_{max}$. ω is a $(\tilde{N}_{max} + 1)$ -dimensional vector on the simplex. $\mu_{\ell_{\tilde{N},i}}$ and $\nu_{\ell_{\tilde{N},i}}$ are two-dimensional vectors – the covariance on locations is diagonal. The latent variables also fully factorize within each tile. Note that in the exact posterior, \tilde{N} has support on the nonnegative integers; in the variational distribution, we truncate at some large N_{max} .

These distributions were taken for convenience: fluxes are positive and right skewed, so we place a normal distribution on log-fluxes; locations are between zero and R , so we place a normal distribution on the logit of the location scaled by $1/R$.

3.1.3 Neural network architecture

In each tile, the distributional parameters in (25), (26), and (27) are the output of a neural network. The input to the neural network is an $R \times R$ tile, padded with surrounding pixels. Padding enables the neural network to produce better predictions inside the tile. For example, a bright source in the vicinity of but outside the tile will affect the pixel values inside the tile. Padding the tiles allows the neural network access to this information. The appropriate amount of padding will depend on the PSF width in the analyzed image. To catalog the crowded starfield M2 (Section 6), we set $R = 2$ and padded the tile with a three-pixel-wide boundary. Thus, while the distribution on tile latent variables factorize over tiles, the neural network is able to use information from neighboring tiles in producing the distributional parameters.

Let $\hat{x}^{(s,t)}$ denote the padded tile pixel intensities (which includes all B bands) and h_η be the neural network, which returns the collection of distributional parameters

$$h_\eta(\hat{x}^{(s,t)}) = (\omega^{(s,t)}, \mu_\ell^{(s,t)}, \nu_\ell^{(s,t)}, \mu_f^{(s,t)}, \sigma_f^{(s,t)}). \quad (28)$$

The same neural network is evaluated for all tiles (s, t) . Our variational parameters are neural network weights, here denoted η . The architecture consists of several convolutional layers followed by a series of fully connected layers (Figure 3). This architecture has been successful on image classification challenges such as ImageNet (Russakovsky et al., 2015). The optimization of the architecture is left for future work; our focus in this paper is the

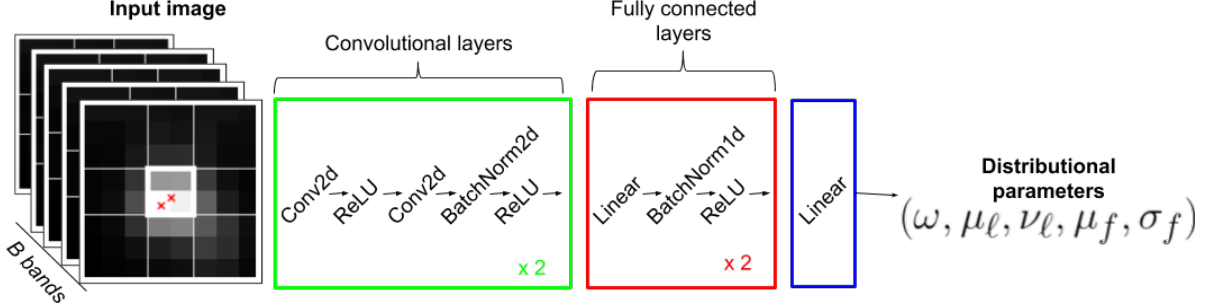


Figure 3: The neural network architecture. For cataloging M2, the input image is an 8×8 padded tile, and the network returns distributional parameters for latent variables contained in the center 2×2 tile.

application of neural networks to provide a variational posterior for cataloging starfields, not the network architecture per se.

Note the output dimension of the neural network. For each tile (s, t) , the categorical parameter $\omega^{(s,t)}$ lies on the simplex and has dimension $N_{max} + 1$. Furthermore, each index of the triangular array $i = 1, \dots, \tilde{N}^{(s,t)}, \tilde{N}^{(s,t)} = 1, \dots, N_{max}$ describes a star. The star has a mean and variance for each location coordinate, and a mean and variance for its flux in each band. Thus, for each star $(\tilde{N}^{(s,t)}, i)$, the neural network outputs $2 \times (B + 2)$ parameters. In total, the neural network has output dimension $(N_{max} + 1) + (B + 2) \times (N_{max}^2 + N_{max})$.

Because the output dimension is quadratic in N_{max} , factorizing the variational distribution spatially keeps the output dimension of the neural network manageable. On a crowded starfield with $H = W = 100$, the number of imaged stars is on the order of 10^3 . If the neural network were to return a variational distribution on the full 100×100 pixel image, the output dimension would be on the order of $(10^3)^2$. On the 2×2 tile, we set $N_{max} = 3$, and the output dimension of the neural network with two bands is 53. With this factorization, the network can be used for inference on an image of any size.

We emphasize that while the variational distribution factorizes over 2×2 tiles, our method does not break the inference problem for the full image into isolated subproblems. The evaluation of the likelihood, e.g., when computing the ELBO in (12), is always on the full image. Light from a star within a 2×2 tile spills over into neighboring tiles, so the likelihood should not and does not decouple across image tiles.

4 The wake-sleep algorithm

In mean-field variational inference, the ELBO (12) is often optimized by coordinate ascent in the parameters of the variational distribution. The coordinate ascent updates can be

derived in closed form in the special case of exponential family models that are conditionally conjugate (Blei et al., 2017).

In our setting of amortized variational inference, stochastic optimization procedures have been employed with modern auto-differentiation tools to avoid the need for deriving analytic updates. Examples include black-box variational inference (BBVI) (Ranganath et al., 2013) and automatic-differentiation variational inference (ADVI) (Kucukelbir et al., 2017). The latter is closely related to the reparameterization trick (Kingma and Welling, 2013; Rezende et al., 2014) proposed to train deep generative models using the KL objective. These approaches all sample latent variables from q_η and produce an unbiased estimate for the gradient of the KL; the optimization is done with stochastic gradient descent.

However, the reparameterization trick does not apply when a latent variable – in our case, the number of stars N – is discrete. The REINFORCE estimator (Williams, 1992), which BBVI adapts, produces an unbiased stochastic gradient for both continuous and discrete latent variables. However, these gradients often suffer from high variance in practice, and so the resulting stochastic optimization is slow. We find this to be true in our application as well (Section 5). See Appendix A for details concerning both the reparameterization and REINFORCE estimators.

The key difficulty in constructing stochastic gradients of the ELBO is that the integrating distribution depends on the optimization parameter η . The *wake-sleep* algorithm, originally proposed by Hinton et al. (1995), replaces the ELBO objective with

$$\mathcal{L}_{\text{sleep}}(\eta) := -\mathbb{E}_{x \sim p(x)} \left[\text{KL}(p(z|x) \| q_\eta(z|x)) \right], \quad (29)$$

known as the *sleep objective*. Section 4.1 details a simple gradient estimator for (29) that does not require reparameterization or REINFORCE.

There are two key differences between the sleep objective (29) and the ELBO (12). First, the KL arguments are transposed. Recall that maximizing the ELBO is equivalent to minimizing $\text{KL}(q \| p)$, and therefore, the minimization of $\text{KL}(q \| p)$ does not depend on the intractable data likelihood $p(x)$. However, the minimization of KL with arguments reversed does. As will be detailed in Section 4.1, the outer expectation over the data in (29) makes this optimization objective tractable without dependence on $p(x)$.

Second, the expectation over the data also gives different meaning to the sleep objective. The ELBO objective seeks η to minimize the KL between $q_\eta(z|x)$ and $p(z|x)$ for *fixed, observed data* x , in this case the $H \times W$ image. In contrast, the sleep objective seeks to minimize the KL *on average over all possible data* x , as weighted by the generative model $p(x)$. In other words, the target is no longer an approximate posterior for the observed data, but rather an approximate posterior that is “good on average” over possible data.

Moreover, “possible data” is defined under the generative model from Section 2. Therefore, it is imperative that the generative model $p(x)$ approximates the true underlying data-generating mechanism well. Thus, in addition to the sleep phase, the wake-sleep algo-

rithm also incorporates a ‘‘wake-phase’’ to estimate model parameters. In our application, these model parameters include the PSF parameters π and background parameters β . Let $\phi := (\pi, \beta)$ be the concatenation of all model parameters, and denote the dependence of the generative model on ϕ using subscripts, p_ϕ .

To estimate model parameters, one would ideally optimize the marginal log-likelihood $\log p_\phi(x)$. However, since $\log p_\phi(x)$ is intractable, the wake-phase optimizes for ϕ using the ELBO objective (12) as a surrogate for the intractable log-likelihood. The ELBO is a lower bound of $\log p_\phi(x)$; it is equal to $\log p_\phi(x)$ when $q_\eta(z|x) = p_\phi(z|x)$.

The *wake-sleep* algorithm thus alternates between the two objectives:

$$\text{Sleep phase: } \eta_t = \arg \max_{\eta} -\mathbb{E}_{x \sim p_\phi(x)} [\text{KL}(p_{\phi_{t-1}}(z|x) \| q_\eta(z|x))]; \quad (30)$$

$$\text{Wake phase: } \phi_t = \arg \max_{\phi} \mathbb{E}_{q_{\eta_t}(z|x)} [\log p_\phi(x, z) - \log q_{\eta_t}(z|x)], \quad (31)$$

for iterations $t = 1, \dots, T$.

Stochastic gradients of the expectation in the wake-phase are simple to compute. Because the integrating distribution does not depend on the optimization parameter ϕ in the wake phase, unbiased stochastic gradients are simply computed as

$$\nabla_\phi \log p_\phi(x, z) \quad \text{for } z \sim q_\eta. \quad (32)$$

Section 4.1 shows that a similarly simple gradient estimator exists for the sleep objective.

The wake-sleep algorithm is closely related to variational EM (Jordan et al., 1999; Neal and Hinton, 2000; Beal and Ghahramani, 2002), which alternates between an *expectation* step (E-step) and a *maximization* step (M-step):

$$\text{E-step: } \eta_t = \arg \max_{\eta} \mathbb{E}_{q_\eta(z|x)} [\log p_{\phi_{t-1}}(x, z) - \log q_\eta(z|x)]; \quad (33)$$

$$\text{M-step: } \phi_t = \arg \max_{\phi} \mathbb{E}_{q_{\eta_t}(z|x)} [\log p_\phi(x, z) - \log q_{\eta_t}(z|x)], \quad (34)$$

for iterations $t = 1, \dots, T$.

Variational EM can be viewed as block coordinate ascent on the ELBO objective, with the E-step optimizing variational parameters η and the M-step optimizing the model parameters ϕ .

The wake phase of the wake-sleep algorithm is equivalent to the M-step of variational EM. As discussed above, the optimization of variational parameters η using the ELBO objective is not conducive to using simple stochastic gradient estimators. Thus, the sleep phase replaces the ELBO objective of the E-step with the expected reverse KL in (29).

4.1 Decomposing the sleep objective

In this section, we decompose the sleep objective in (29) for closer study. We take ϕ as fixed in this section and drop the explicit dependence of p on ϕ .

First, observe that optimizing the sleep objective does not require computing the intractable term $p(x)$:

$$\arg \max_{\eta} \mathcal{L}_{\text{sleep}}(\eta) = \arg \min_{\eta} \mathbb{E}_{x \sim p(x)} \left[\text{KL}(p(z|x) \| q_{\eta}(z|x)) \right] \quad (35)$$

$$= \arg \min_{\eta} \mathbb{E}_{p(x)} \left[\mathbb{E}_{p(z|x)} \left(\log p(z|x) - \log q_{\eta}(z|x) \right) \right] \quad (36)$$

$$= \arg \min_{\eta} \mathbb{E}_{p(x)} \left[\mathbb{E}_{p(z|x)} \left(-\log q_{\eta}(z|x) \right) \right] \quad (37)$$

$$= \arg \min_{\eta} \mathbb{E}_{p(x,z)} \left[-\log q_{\eta}(z|x) \right]. \quad (38)$$

Crucially, the integrating distribution, $p(x, z)$, does not depend on the optimization parameter η . In the E-step of variational EM, the integrating distribution is q_{η} , resulting in the need for reparameterization or other adjustments to compute stochastic gradients. Here, unbiased stochastic gradients can be obtained simply as

$$g = -\nabla_{\eta} \log q_{\eta}(z|x) \quad \text{for } (z, x) \sim p(x, z). \quad (39)$$

In other words, the sleep phase simulates *complete* data (z, x) from the generative model and evaluates the loss $-\log q_{\eta}(z|x)$. Here, “complete data” refers to the image along with its catalog. This loss encourages the neural network to map an image x to a distribution $q_{\eta}(\cdot|x)$ that places large mass on the image’s catalog z .

Furthermore, recall that q_{η} factorizes over image tiles. Having sampled the catalog z and the $H \times W$ image x from $p(x, z)$, convert z to its tile parameterization $(\tilde{N}^{(s,t)}, \tilde{\ell}^{(s,t)}, \tilde{f}^{(s,t)})_{s=1,t=1}^{(S,T)}$, as detailed in Section 3.1.1.

For a given image tile, the latent variables $\tilde{N}^{(s,t)}$, $\tilde{\ell}^{(s,t)}$, and $\tilde{f}^{(s,t)}$ also factorize in q , so

$$-\log q_{\eta}(\tilde{N}^{(s,t)}, \tilde{\ell}^{(s,t)}, \tilde{f}^{(s,t)}|x) = -\log q_{\eta}(\tilde{N}^{(s,t)}|x) - \log q_{\eta}(\tilde{\ell}^{(s,t)}|x) - \log q_{\eta}(\tilde{f}^{(s,t)}|x). \quad (40)$$

Each term can be interpreted separately. In tile (s, t) , the number of stars $\tilde{N}^{(s,t)}$ is categorical with parameter $\omega^{(s,t)}$. The loss function for the number of stars becomes

$$-\log q_{\eta}(\tilde{N}^{(s,t)}|x) = -\sum_{n=0}^{\tilde{N}_{\max}} \mathbb{1}\{\tilde{N}^{(s,t)} = n\} \log \omega_n^{(s,t)}, \quad (41)$$

the usual cross-entropy loss for a multi-class classification problem.

Recall that location coordinates are logit-normal and fluxes are log-normal in the last two terms in (40). For a given index (n, i) , let $y_{n,i}$ generically denote either the logit-location or log-flux for that star, and let $\mu_{n,i}$ and $\sigma_{n,i}$ generically denote the mean and standard deviation of its Gaussian variational distribution. Thus,

$$-\log q_{\eta}(y_{n,i}|x) = \frac{1}{2\sigma_{n,i}^2} (y_{n,i} - \mu_{n,i})^2 + \log \sigma_{n,i} + \frac{1}{2} \log(2\pi). \quad (42)$$

By our discussion in Section 3.1.1, only the $N = N^{(s,t)}$ -th row of the triangular array of latent variables $\tilde{\ell}^{(s,t)}$ and $\tilde{f}^{(s,t)}$ needs to be evaluated. Therefore, the losses in the last two terms of (40) are of the form

$$-\log q_\eta(y|x) = -\sum_{i=1}^{\tilde{N}^{(s,t)}} \log q_\eta(y_{\tilde{N}^{(s,t)},i}|x). \quad (43)$$

To interpret (42), observe that $y_{n,i}$ is the true (simulated) latent variable in the catalog and $\mu_{n,i}$ is the predicted value for that latent variable from the neural network. $\sigma_{n,i}$ is also outputted by the neural network, representing uncertainty – the second term encourages small uncertainties, but this is balanced by the scaling of the error $(y_{n,i} - \mu_{n,i})^2$ in the first term.

The losses in (41) and (42) show that the sleep objective results in a supervised learning problem on complete data simulated from our generative model: the objective function for the number of stars is the usual cross-entropy loss for classification, while the objective function for log-fluxes and logit-locations are L_2 losses in the mean parameters.

5 Empirical comparison of ELBO optimization and sleep optimization

A simple example demonstrates that there exist shallow local optima in the ELBO where the fitted approximate posterior is far in KL divergence from the exact posterior. These local optima result in unreliable catalogs. The sleep objective, by taking advantage of complete data, appears to better avoid these local optima. For this example, the data were simulated with known PSF and background, and the wake phase is not needed.

The simulated 20×20 single-band image x_{test} is shown in Figure 4. The image has four stars, each with the same flux.

We compare three approaches to deblending. The first two approaches directly optimize the test ELBO,

$$\mathcal{L}_{elbo}(\eta; x_{test}) = \mathbb{E}_{q_\eta(z|x_{test})} \left[\log p(x_{test}, z) - \log q_\eta(z|x_{test}) \right], \quad (44)$$

while the third approach optimizes the sleep objective (29). In each case, q_η is the inference network from Section 3.1.3; the input to the network is a 10×10 tile with no padding.

Note that the sleep objective does not depend on x_{test} . Optimizing the sleep objective only requires sampling catalogs from the prior and simulating images conditional on each catalog. The prior on the number of stars was set to Poisson with mean $\mu = 4$.

Figure 5 (top row) charts the test ELBO (44) as the optimization proceeds in our three approaches. The first approach optimizes the ELBO with stochastic gradient descent and

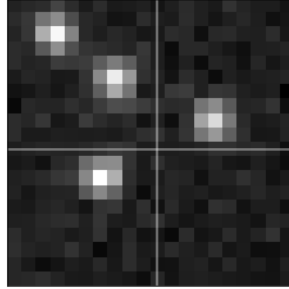


Figure 4: The 20×20 pixel synthetic image x_{test} . It contains four stars and is partitioned into 10×10 tiles.

the REINFORCE gradient estimator. This optimization did not converge, likely due to the high variance of the REINFORCE estimator (Figure 5a). For a lower variance gradient estimator, the second approach employed the reparameterized gradient. To employ this gradient estimator, we analytically integrated the ELBO with respect to the number of stars N to remove the discrete random variable. See Appendix A for details about the gradient estimators. Using reparameterized gradients instead of REINFORCE gradients enabled the optimization to converge to stationary points (Figure 5b). However, for two of the six randomly initialized restarts, the optimization found local optima where the negative ELBO is higher than other restarts.

In contrast, optimizing the sleep objective consistently converged to a similar ELBO across all restarts and appeared to avoid shallow local optima (Figure 5c). Recall that sleep phase optimization does not directly optimize the test ELBO. However, the test ELBO increases nonetheless, because the variational posterior better approximates the exact posterior as the optimization proceeds.

Shallow local optima in the ELBO result in unreliable catalogs. The bottom row of Figure 5 displays the estimated locations, defined as the mode of the fitted variational distribution. The bottom left shows these locations after converging to a shallow local optimum. In this local optimum, the upper left tile was correctly estimated to have two stars; however, both estimated stars were placed at the same location. For correct detections, one of the locations should be placed on the second star. However, in order to move one of the estimated locations to the second star, the optimization path must traverse a region where the log-likelihood is lower than the current configuration (Figure 6). The displayed configuration is a local optimum where the gradient with respect to its locations is approximately zero. In contrast, the sleep-phase variational distribution consistently placed its mode around the four true stars. The sleep objective is quadratic in the logit-location estimate μ_ℓ (Equation 42), and the gradient does not vanish in the sleep objective. An example of correct detection after sleep-phase optimization is shown in the bottom right

image of Figure 5.

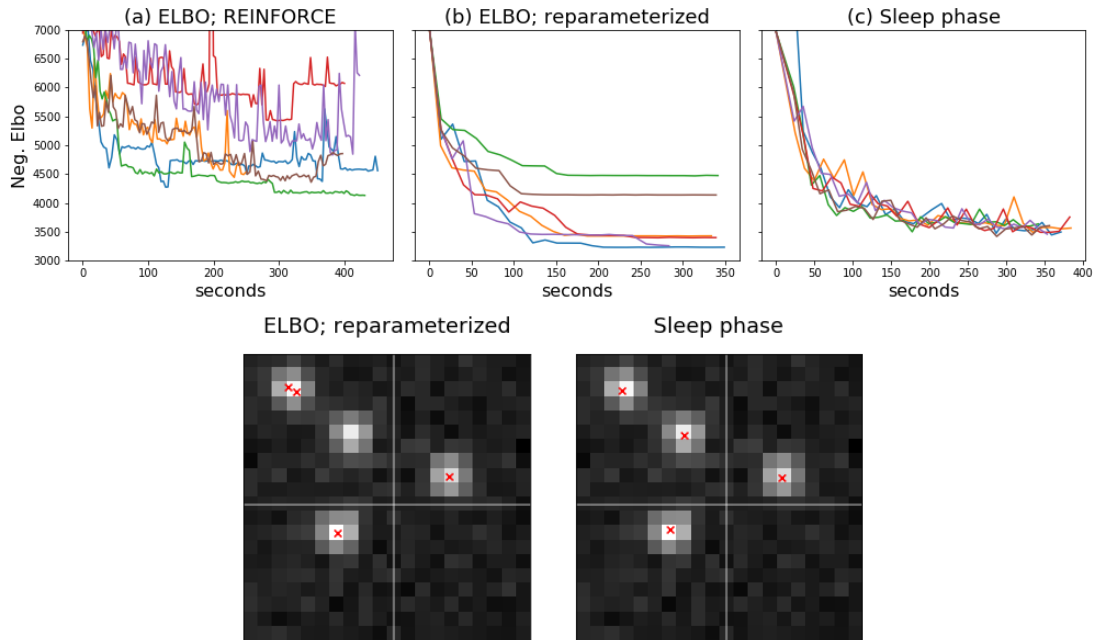


Figure 5: (Top row) The ELBO as the optimization progresses for six random restarts. (Bottom row) Modal locations from two variational posteriors in red. On the left, a randomly initialized run where optimizing the ELBO with the reparameterized gradient resulted in a shallow local optimum: the estimated locations split a single source into two sources, while missing another source entirely. On the right, the variational posterior was optimized using the sleep phase and correctly identified all four sources.

Also, note that low-variance gradients of the ELBO for this simple example were constructed by analytically integrating out N . Only then could the reparameterization trick be applied to the ELBO, as the remaining latent variables are continuous. In this example, the variational distribution has support over only 0, 1, or 2 stars for each tile. Since the variational distribution factorizes over the four tiles, integrating N is a summation of $3^4 = 81$ terms. On larger images with more tiles, analytically integrating N would be computationally infeasible, and the simple reparameterization trick would not apply as it does in this small illustrative example.

Figure 7 displays our results on a larger example: a simulated 100×100 pixel image with fifty stars. The tiles again consisted of 10×10 pixel regions. Optimizing the ELBO does not produce accurate location estimates and appears to be hindered by regions with little gradient information; optimizing the sleep objective produced much improved location estimates.

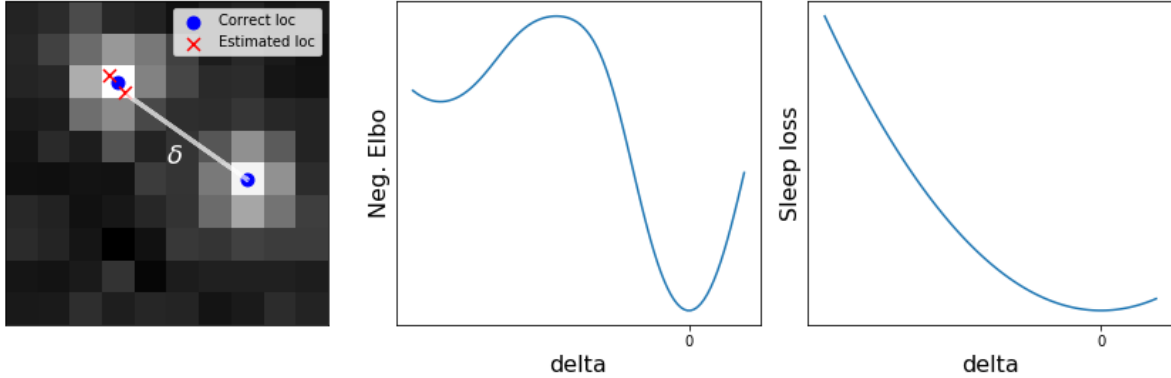


Figure 6: An illustration of local optima in the ELBO objective. To move an estimated location to a correct location, the optimization path must traverse a region where the negative ELBO is larger than the current configuration. In contrast, the sleep objective is quadratic in the estimated location, and the gradient does not vanish.

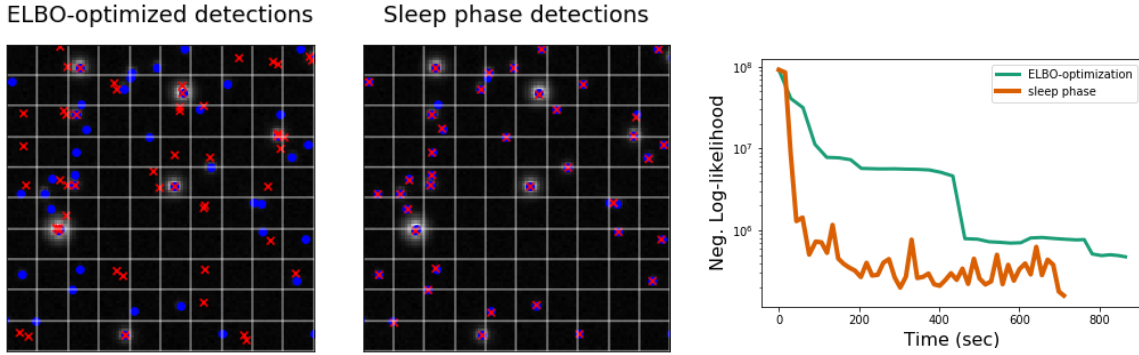


Figure 7: (Left) Detections produced by ELBO optimization on a 100×100 pixel test image. Correct locations are blue and estimated locations are red. (Middle) Detections produced by the sleep phase optimization. (Right) The negative conditional log-likelihood, $-\log p(x|\hat{z})$, where \hat{z} is the mode of the variational posterior and x the 100×100 pixel test image.

6 Results on the M2 globular cluster

We validated StarNet using an SDSS image of the Messier 2 (M2) globular cluster, a crowded starfield found in field 136 of camera column 2 in run 2583. M2 was also imaged in the ACS Globular Cluster Survey (Sarajedini et al., 2007) using the Hubble Space telescope (HST), which has greater resolution than the Sloan telescope (0.05 arcseconds per pixel and 0.4 arcseconds per pixel, respectively; see ESAHubble (2021) and SDSS (2020)). The reported catalog from this Hubble survey serves as the ground truth for validating our results.

We consider the 100×100 pixel subimage of M2 that Portillo et al. (2017) and Feder et al. (2020) analyzed with PCAT. This subimage is located approximately two arcseconds from the heavily saturated core of the cluster; even in this subimage, the HST catalog contains over 1000 stars with F606W-band magnitudes less than 22.

Both StarNet and PCAT are able to model multiband images. We include two bands in our analysis, the SDSS *r*-band and *i*-band. The SDSS *r*-band and the Hubble F606W band are centered at roughly the same wavelength, but the wavelength range of the Hubble F606W band is slightly broader.

6.1 Runtime

We factorized our variational distribution into 2×2 pixel tiles. The neural network inputs were 8×8 pixel padded tiles: 2×2 tiles along with three surrounding pixels of padding (see Figure 3). The SDSS estimates for the PSF and background were used in the first sleep phase. This phase ran for 200 epochs; at each epoch, 200 images were sampled from the generative model. Optimization was done with Adam (Kingma and Ba, 2014). On a single NVIDIA GeForce RTX 2080 Ti GPU, the initial sleep phase took 15.2 minutes.

Two additional wake-sleep cycles followed the first sleep phase, after which the model parameters and inferred catalog appeared stable. The subsequent sleep phases were shorter (10 epochs with 200 images each), and the wake phase employed SGD, with the gradient estimator (32). In total, the two further wake-sleep cycles took three minutes.

After fitting the model and variational posterior, calculating the approximate posterior (that is, producing the distributional parameters of the variational approximation) for the 100×100 pixel image of M2 took 30 milliseconds. By comparison, the reported runtime of PCAT, which uses MCMC, is 30 minutes on the same 100×100 pixel image (Feder et al., 2020). In other words, after the initial fit, StarNet provided nearly a 10^5 -fold speed increase.

The speed at inference time (which excludes training time) gives StarNet the scaling characteristics necessary for processing large astronomical surveys. A single SDSS image is 1489×2048 pixels. Based on the reported 30-minute runtime of PCAT for a 100×100 pixel subimage, we project that the runtime to process the full image would be $30 \text{ min} \times 14 \times 20 = 8400$ minutes, or almost six days. The SDSS survey consists of nearly one million images. Scaling PCAT to the entire SDSS survey would be infeasible. The upcoming LSST survey will be 300 times larger than SDSS.

In contrast, if we assume the PSF and background are homogeneous across the full SDSS image (which is also assumed in PCAT), we can fit StarNet using wake-sleep on a small 100×100 pixel subimage (while simultaneously obtaining estimates of the PSF and background), a one time computational cost of 18.2 minutes. Producing a catalog with the full 1489×2048 pixel image requires $30 \text{ msec} \times 14 \times 20 = 8.4$ seconds. In practice, inference

can be made even faster by batching the image tiles to run in parallel on a GPU.

6.2 Inference

The cataloging accuracy of StarNet is compared with PCAT and DAOPHOT (Stetson, 1987). DAOPHOT is an algorithmic routine for detecting stars in crowded starfields which does not use a generative model. This software convolves the observed image with a Gaussian kernel and scans for peaks above a given threshold. The DAOPHOT catalog of M2 was reported in An et al. (2008).

To evaluate the three methods, the HST catalog was used as ground truth. We filtered the HST catalog to stars with magnitudes smaller than 22.5 in the Hubble F606W band, because stars with lower apparent brightness cannot be detected in SDSS images.

Estimated catalogs are evaluated on three metrics: the true positive rate (TPR), the positive predicted value (PPV), and the F1 score. The TPR is the proportion of stars in the HST catalog matched with a star in the estimated catalog; the PPV is the proportion of stars in the estimated catalog matched with a star in the HST catalog. The F1 score summarizes the two metrics as the harmonic mean of the PPV and the TPR.

Like Portillo et al. (2017) and Feder et al. (2020), a “match” between an estimated star and an HST star is defined as follows: (1) the estimated location and the HST location are within 0.5 SDSS pixels, and (2) the estimated SDSS r -band flux and the HST F606W band flux are within half a magnitude.

In probabilistic cataloging (PCAT and StarNet), the posterior defines a distribution over catalogs. For StarNet, the TPR, PPV, and F1 score were computed for the catalog corresponding to the mode of the variational distribution (henceforth, the StarNet catalog). For PCAT, 300 catalogs were sampled using MCMC; the metrics were computed for each sampled catalog and averaged.

Fitting StarNet using wake-sleep (StarNet-WS) resulted in a catalog that outperforms DAOPHOT and PCAT in terms of its F1 score (Table 1). Fitting StarNet without the wake phase and using only the default SDSS background and PSF (StarNet-S) produced a catalog with a TPR similar to that of StarNet-WS but with a smaller PPV. PCAT estimated the most stars of all methods; it therefore had a large TPR but a small PPV. On the other hand, DAOPHOT estimated less than half the number of stars when compared to the other methods. It therefore had a large PPV but a small TPR. The StarNet-WS catalog had about the same PPV as DAOPHOT while having nearly the same TPR as PCAT.

Table 1 also prints the number of stars inferred by each method. For probabilistic methods (StarNet and PCAT), we display the mean number of stars under the approximate posterior, along with the 5-th and 95-th quantiles. Neither PCAT nor StarNet captured the true number of stars in their 90% credible interval, though StarNet-WS came the closest.

Table 1: Performance metrics on M2. In the bottom row, “Hubble” refers to the catalog which we use as ground-truth. For probabilistic methods (StarNet and PCAT) the “#stars” column refers to the mean number of stars under the (approximate) posterior, while the right-most column displays the 5-th and 95-th percentiles under the posterior.

Method	TPR	PPV	F1 score	#stars	(q-5%, q-95%)
DAOPHOT	0.20	0.63	0.30	295	—
PCAT	0.56	0.40	0.47	1672	(1664, 1680)
Sleep-only	0.51	0.47	0.49	1292	(1260, 1324)
Wake-sleep	0.51	0.60	0.55	1014	(987, 1041)
Hubble	1.00	1.00	1.00	1114	—

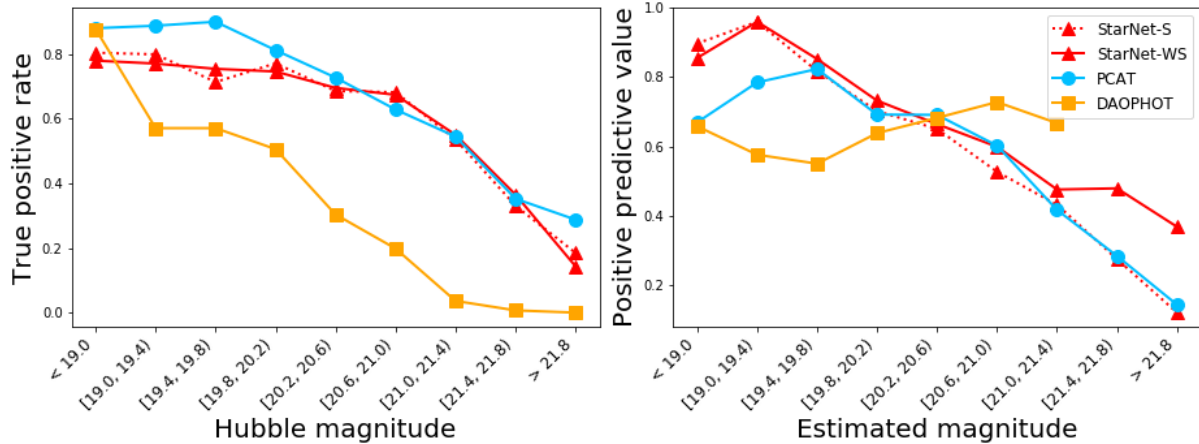


Figure 8: True positive rate (left) and positive predicted value (right) of various cataloguing procedures on M2, plotted against r -band magnitude. Smaller magnitudes correspond to brighter stars.

The StarNet credible intervals were three times wider than the PCAT intervals. The small PCAT credible intervals may be indicative of an MCMC sampler that failed to mix well.

The improvement of StarNet-WS in PPV was most pronounced for dim stars (Figure 8). The TPR for StarNet-WS was uniformly better than DAOPHOT for stars of all magnitudes. Of all methods, the StarNet-WS catalog best approximated the Hubble flux distribution (Figures 9 and 10). PCAT overestimated the number of dim stars with magnitudes greater than 21. In contrast, DAOPHOT failed to find dim stars; its flux distribution assigned zero probability to stars with magnitudes greater than 21.

The difference between the source-magnitude histograms (Figure 10) produced by StarNet-WS and PCAT is likely due to the fact that StarNet-WS estimates the background with maximum likelihood, while the background in PCAT is fixed. As discussed below, the

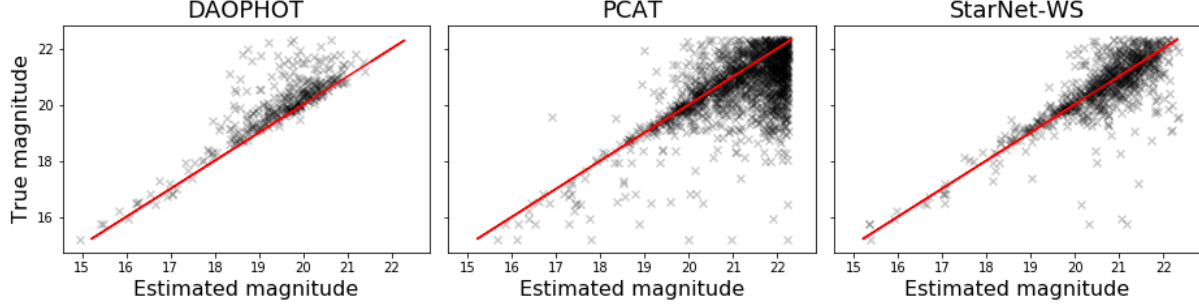


Figure 9: True versus estimated magnitudes on the r -band of M2. Every estimated star was matched with the nearest Hubble star in L2 distance between locations. Red line is the identity, $y = x$.

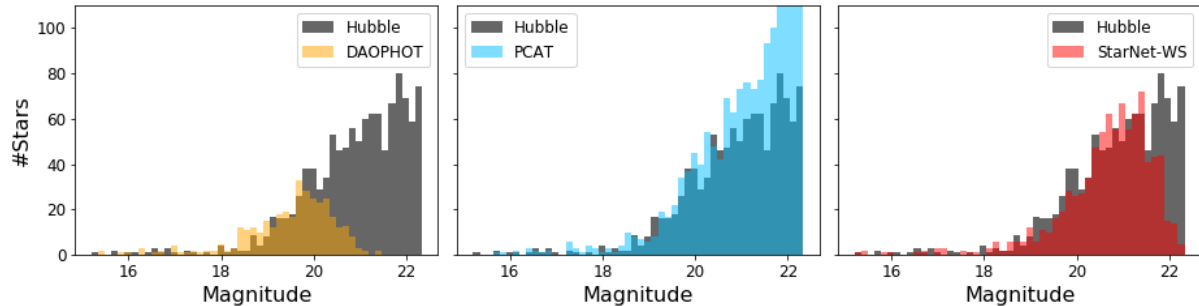


Figure 10: Source magnitude histograms for the r -band observations of M2. The magnitude distribution of the Hubble catalog in grey. Magnitude distributions for the DAOPHOT, PCAT, and StarNet-WS catalogs overlaid. For PCAT, the magnitude histogram plotted is from a single catalog sampled by MCMC. PCAT overestimates the number of dim sources, while DAOPHOT fails to detect dim sources.

SDSS estimate of the background (which PCAT uses) is too dim, and PCAT compensates for the model mis-match by estimating more dim stars. The StarNet-WS estimate increases the intensity of the background, and hence does not over-estimate dim stars.

Figure 11 shows the StarNet-WS catalog alongside PCAT, DAOPHOT, and Hubble catalogs.

StarNet-WS returns a well-defined distribution over the set of all catalogs and is thus able to capture uncertainties in catalog construction. Samples from the StarNet-WS variational distribution are compared with samples from PCAT in Figure 12. To examine the uncertainty calibration of StarNet-WS, we evaluated the approximate posterior conditional on the true number of stars in the Hubble catalog. Then, each star in the StarNet-WS catalog was matched with exactly one Hubble star by finding the permutation of Hubble stars that had the largest log-likelihood under our variational distribution q_η . For each

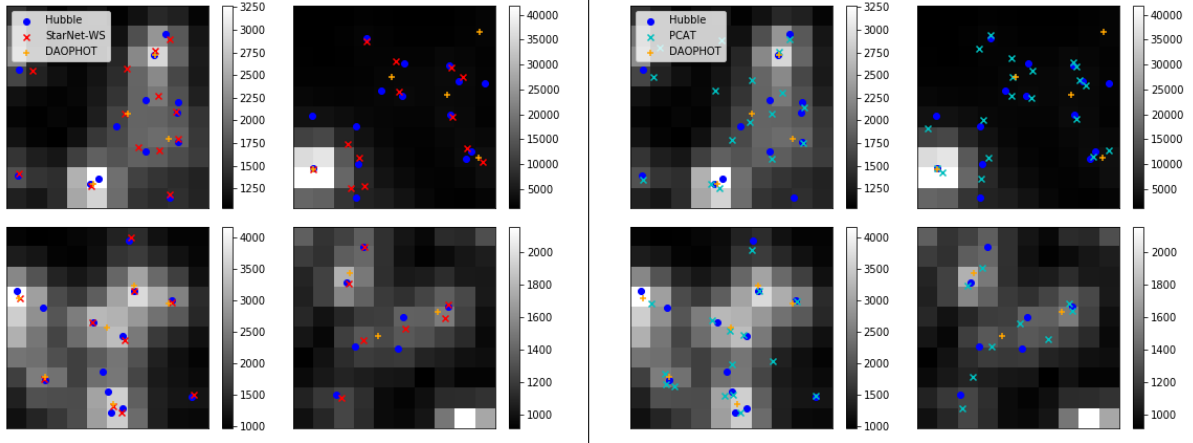


Figure 11: Estimated catalogs on four 10×10 subimages from M2. Blue dots are stars from the Hubble catalog used as ground truth. Starnet-WS, PCAT, and DAOPHOT estimated stars are shown as red, cyan, and orange crosses, respectively.

star, we computed the z-score $(y - \hat{y})/\hat{\sigma}$, where y is the Hubble log-flux or logit-location; \hat{y} and $\hat{\sigma}$ are the mean and the standard deviation, respectively, of the Gaussian variational distribution for the log-flux or logit-location. If the uncertainties were perfectly calibrated, the distribution of these z-scores would be a standard Gaussian. The empirical z-score distributions are close to a standard Gaussian with some discrepancy in the tails and some evidence of unmodeled skewness, suggesting the uncertainties are not too mis-estimated (Figure 13).

Finally, we evaluate the quality of the wake-phase estimates for the PSF and background. Let z_h denote the Hubble catalog, and given some model parameters ϕ , let

$$\mathcal{L}^{Hubble}(\phi) := -\log p_\phi(x^{(r)}|z_h) \quad (45)$$

be the negative log-likelihood of the SDSS r -band image conditional on the Hubble catalog (recall that the Hubble absorption range most closely resembles the SDSSgit c r -band). The log-likelihood of model parameters estimated by the wake phase is nearly four times larger than the log-likelihood of parameters estimated by SDSS (Table 2). The largest improvement in log-likelihood came from the wake-estimated background, which was brighter than the SDSS background, suggesting that the SDSS background was too dim for this starfield.

Appendix B presents the results of StarNet, PCAT, and DAOPHOT on a neighboring 100×100 pixel subimage of M2. The results remain qualitatively similar in that StarNet has the best F1 score of all methods. Importantly, StarNet was applied to the new region without further wake-sleep optimization; StarNet produced a catalog on this new region in ≈ 30 milliseconds. On the other hand, PCAT required a new 30 minute run of MCMC.

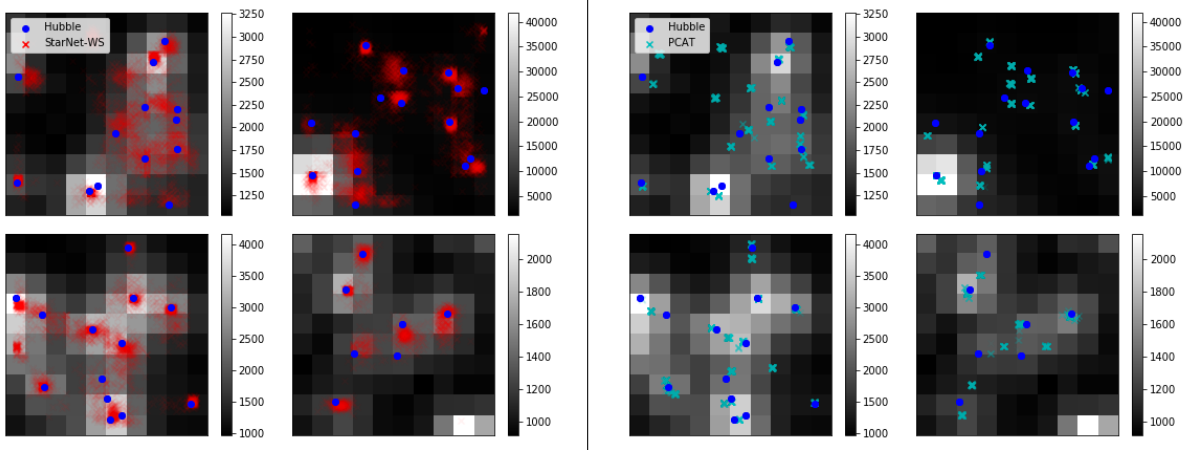


Figure 12: Four 10×10 subimages from M2. Blue dots are stars from the HST catalog used as ground truth. (Left) Posterior samples from StarNet-WS and (right) posterior samples from the MCMC chain of PCAT.

Table 2: The negative log-likelihood (45) for various model estimates. PHOTO provides estimates of background and PSF for every SDSS data release. We compare the PHOTO estimates with StarNet estimates obtained after two cycles of wake-sleep.

Model estimate		Neg.Loglik
background	PSF	
PHOTO	PHOTO	8.671e+05
PHOTO	StarNet	8.665e+05
StarNet	PHOTO	3.651e+05
StarNet	StarNet	3.395e+05

7 Conclusion

StarNet employs variational inference and outperforms both an MCMC-based probabilistic cataloger and a non-model-based approach in terms of accuracy and runtime. Under the framework of probabilistic modeling, StarNet produces catalogs in which uncertainties are captured by a Bayesian posterior over the set of all catalogs. Importantly, unlike MCMC, StarNet also has the capacity to scale probabilistic cataloging to process large astronomical surveys.

The quality of StarNet detections is the result of optimizing the forward KL, a different objective than the one traditionally used in variational inference. Optimizing the forward KL allows the variational posterior to be fit on large amounts of *complete* data – the image along with its latent catalog – generated from the statistical model. While labeled

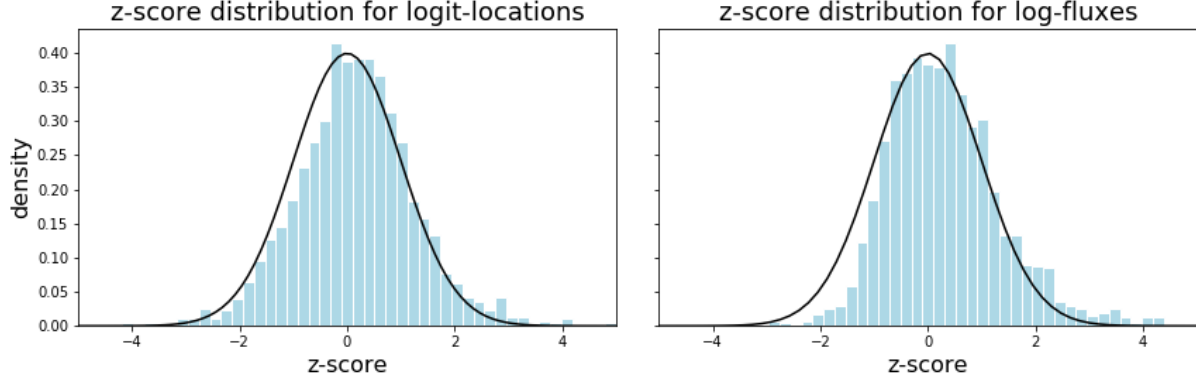


Figure 13: The empirical distribution of z-scores for logit-locations (left) and log-fluxes (right) under the StarNet-WS variational posterior.

data from simulators has been used in other astronomy applications to train deep neural networks (see for example Lanusse et al. (2017) and Huang et al. (2020)), StarNet is the first training procedure to employ simulated data in a statistical framework: the neural network specifies an approximate Bayesian posterior.

This variational approach, unlike previous MCMC approaches, enables StarNet to estimate model parameters such as the PSF and sky background. While the current work focuses on PSF models, our methodology can be extended to more general sources such as galaxies. Unsurprisingly, the current performance of StarNet is sub-optimal for cataloging regions of the sky that contain both stars and galaxies, due to model misfit (Appendix D).

One promising direction is using a neural network for the generative model and fitting a deep generative model for galaxies (Regier et al., 2015; Reiman and Göhre, 2019; Lanusse et al., 2020; Arcelin et al., 2021). Here, a neural network encodes a conditional likelihood of galaxy images given a low-dimensional galaxy representation. Using a neural network to encode a likelihood extends the flexibility of galaxy models beyond the simple models used here.

The statistical framework in this research lays the foundation for building flexible models to incorporate the cataloging of all celestial objects. Future astronomical surveys will only expand in terms of the volume of data they are able to amass. As telescopes peer deeper into space, fields will reveal more sources and images will become more crowded. The uncertainties in crowded fields necessitate a probabilistic approach. Our method holds the promise of providing a scalable inference tool that can meet the challenges of these future surveys.

References

Abbott, T. M., Abdalla, F. B., Alarcon, A., et al. (2018), “Dark Energy Survey Year 1 Results: Cosmological Constraints from Galaxy Clustering and Weak Lensing,” *Physical Review D*, 98.

An, D., Johnson, J. A., Clem, J. L., et al. (2008), “Galactic Globular and Open Clusters in the Sloan Digital Sky Survey. I. Crowded-Field Photometry and Cluster Fiducial Sequences in ugriz,” *The Astrophysical Journal Supplement Series*, 179, 326–354.

Arcelin, B., Doux, C., Aubourg, E., Roucelle, C., and LSST Dark Energy Science Collaboration (2021), “Deblending Galaxies with Variational Autoencoders: a Joint Multiband, Multi-instrument Approach,” *Monthly Notices of the Royal Astronomical Society*, 500, 531–547.

Beal, M. and Ghahramani, Z. (2002), “The Variational Bayesian EM Algorithm for Incomplete Data: with Application to Scoring Graphical Model Structures,” *Bayesian Statistics*.

Blei, D. M., Kucukelbir, A., and McAuliffe, J. D. (2017), “Variational Inference: A Review for Statisticians,” *Journal of the American Statistical Association*, 112, 859–877.

Bornschein, J. and Bengio, Y. (2014), “Reweighted Wake-Sleep,” <https://arxiv.org/abs/1406.2751>.

Bosch, J., Armstrong, R., Bickerton, S., et al. (2018), “The Hyper Suprime-Cam Software Pipeline,” *Publications of the Astronomical Society of Japan*, 70, 1–39.

Brewer, B. J., Foreman-Mackey, D., and Hogg, D. W. (2013), “Probabilistic Catalogs for Crowded Stellar Fields,” *The Astronomical Journal*, 146, 7–15.

ESA Hubble (2021), “Hubble’s instruments: ACS – Advanced Camera for Surveys,” <https://esahubble.org/about/general/instruments/acs/>, [Accessed: 2021-02-21].

Feder, R. M., Portillo, S. K. N., Daylan, T., and Finkbeiner, D. (2020), “Multiband Probabilistic Cataloging: a Joint Fitting Approach to Point-source Detection and Deblending,” *The Astronomical Journal*, 159, 163–188.

Green, G. M., Schlafly, E., Zucker, C., Speagle, J. S., and Finkbeiner, D. (2019), “A 3D Dust Map Based on Gaia, Pan-STARRS 1, and 2MASS,” *The Astrophysical Journal*, 887, 93–120.

Green, P. J. (1995), “Reversible Jump Markov chain Monte Carlo Computation and Bayesian Model Determination,” *Biometrika*, 82, 711–732.

Hinton, G. E., Dayan, P., Frey, B. J., and Neal, R. M. (1995), “The Wake-sleep Algorithm for Unsupervised Neural Networks,” *Science*, 268, 1158–1161.

Huang, X., Domingo, M., Pilon, A., et al. (2020), “Finding Strong Gravitational Lenses in the DESI DECam Legacy Survey,” *The Astrophysical Journal*, 894, 78–106.

Jordan, M. I., Ghahramani, Z., Jaakkola, T. I., and Saul, L. K. (1999), “An Introduction to Variational Methods for Graphical Models,” *Machine Learning*, 37, 183–233.

Kingma, D. P. and Ba, J. (2014), “Adam: a Method for Stochastic Optimization,” <https://arxiv.org/abs/1412.6980>.

Kingma, D. P. and Welling, M. (2013), “Auto-Encoding Variational Bayes,” <https://arxiv.org/abs/1312.6114>.

Kucukelbir, A., Tran, D., Ranganath, R., Gelman, A., and Blei, D. M. (2017), “Automatic Differentiation Variational Inference,” *Journal of Machine Learning Research*, 18, 1–45.

Lanusse, F., Ma, Q., Li, N., Collett, T. E., Li, C.-L., Ravanbakhsh, S., Mandelbaum, R., and Póczos, B. (2017), “CMU DeepLens: deep learning for automatic image-based galaxy–galaxy strong lens finding,” *Monthly Notices of the Royal Astronomical Society*, 473, 3895–3906.

Lanusse, F., Mandelbaum, R., Ravanbakhsh, S., Li, C.-L., Freeman, P., and Poczos, B. (2020), “Deep Generative Models for Galaxy Image Simulations,” <https://arxiv.org/abs/2008.03833>.

Le, T. A., Kosiorek, A. R., Siddharth, N., Teh, Y. W., and Wood, F. (2020), “Revisiting Reweighted Wake-sleep for Models with Stochastic Control Flow,” in *Uncertainty in Artificial Intelligence*, pp. 1039–1049.

LSST (2020), “About LSST,” <https://www.lsst.org/about/dm>, [Accessed: 2020-12-01].

Lupton, R., Gunn, J. E., Ivezić, Z., Knapp, G. R., Kent, S., and Yasuda, N. (2001), “The SDSS Imaging Pipelines,” <https://arxiv.org/abs/astro-ph/0101420>.

Neal, R. and Hinton, G. (2000), “A View Of The EM Algorithm That Justifies Incremental, Sparse, And Other Variants,” *Learning in graphical models*, 89, 355–368.

Portillo, S. K. N., Lee, B. C. G., Daylan, T., and Finkbeiner, D. P. (2017), “Improved Point-source Detection in Crowded Fields Using Probabilistic Cataloging,” *The Astronomical Journal*, 154, 132–156.

Ranganath, R., Gerrish, S., and Blei, D. M. (2013), “Black Box Variational Inference,” <https://arxiv.org/abs/1401.0118>.

Regier, J., McAuliffe, J. D., and Prabhat (2015), “A deep generative model for astronomical images of galaxies,” in *NIPS Workshop on Advances in Approximate Bayesian Inference*.

Regier, J., Miller, A. C., Schlegel, D., Adams, R. P., McAuliffe, J. D., and Prabhat (2019), “Approximate Inference for Constructing Astronomical Catalogs from Images,” *The Annals of Applied Statistics*, 13, 1884–1926.

Reiman, D. M. and Göhre, B. E. (2019), “Deblending Galaxy Superpositions with Branched Generative Adversarial Networks,” *Monthly Notices of the Royal Astronomical Society*, 485, 2617–2627.

Rezende, D. J., Mohamed, S., and Wierstra, D. (2014), “Stochastic Backpropagation and Approximate Inference in Deep Generative Models,” <https://arxiv.org/abs/1401.4082>.

Russakovsky, O., Deng, J., Su, H., Krause, J., Satheesh, S., Ma, S., Huang, Z., Karpathy, A., Khosla, A., Bernstein, M., Berg, A. C., and Fei-Fei, L. (2015), “ImageNet Large Scale Visual Recognition Challenge,” *International Journal of Computer Vision (IJCV)*, 115, 211–252.

Sarajedini, A., Bedin, L. R., Chaboyer, B., Dotter, A., Siegel, M., Anderson, J., Aparicio, A., King, I., Majewski, S., Marín-Franch, A., et al. (2007), “The ACS Survey of Galactic Globular Clusters,” *The Astronomical Journal*, 133, 1658–1672.

Schlafly, E. F., Green, G. M., Lang, D., et al. (2018), “The DECam Plane Survey: Optical Photometry of Two Billion Objects in the Southern Galactic Plane,” *The Astrophysical Journal Supplement Series*, 234, 39–58.

SDSS (2020), “SDSS Scope,” <https://www.sdss.org/dr16/scope/>, [Accessed: 2020-12-23].

Stetson, P. B. (1987), “DAOPHOT: A Computer Program for Crowded-Field Stellar Photometry,” *Astronomical Society of the Pacific*, 99, 191–222.

Wainwright, M. J. and Jordan, M. I. (2008), “Graphical Models, Exponential Families, and Variational Inference,” *Foundations and Trends in Machine Learning*, 1, 1–305.

Williams, R. J. (1992), “Simple Statistical Gradient-Following Algorithms for Connectionist Reinforcement Learning,” *Machine Learning*, 8, 229–256.

Wright, E. L., Eisenhardt, P. R. M., Mainzer, A. K., et al. (2010), “The Wide-field Infrared Survey Explorer (WISE): Mission Description and Initial On-orbit Performance,” *The Astronomical Journal*, 140, 1868–1881.

Xin, B., Ivezić, Z., Lupton, R. H., Peterson, J. R., Yoachim, P., Jones, R. L., Claver, C. F., and Angeli, G. (2018), “A Study of the Point-spread Function in SDSS Images,” *The Astronomical Journal*, 156, 222–232.

Zhang, C., Bütepage, J., Kjellström, H., and Mandt, S. (2019), “Advances in Variational Inference,” *IEEE Transactions on Pattern Analysis and Machine Intelligence*, 41, 2008–2026.

A Reparameterized and REINFORCE gradients

The ELBO objective (12) is of the form

$$\mathcal{L}(\eta) = \mathbb{E}_{q_\eta(z)}[f_\eta(z)]. \quad (46)$$

The parameter η is to be optimized, and z is the latent variable. The integrating distribution q and the function f depend on η .

The REINFORCE estimator Williams (1992) is a general-purpose unbiased estimate for the gradient of (46). It is given by

$$g_{\text{rf}}(z) = \nabla_\eta f_\eta(z) + f_\eta(z) \nabla_\eta \log q_\eta(z) \quad \text{for } z \sim q_\eta(z). \quad (47)$$

The REINFORCE estimate is unbiased for the true gradient:

$$\mathbb{E}_{q_\eta(z)}[g_{\text{rf}}(z)] = \int q_\eta(z) \nabla_\eta f_\eta(z) dz + \int q_\eta(z) f_\eta(z) \nabla_\eta \log q_\eta(z) dz \quad (48)$$

$$= \int q_\eta(z) \nabla_\eta f_\eta(z) dz + \int f_\eta(z) \nabla_\eta q_\eta(z) dz \quad (49)$$

$$= \int \nabla_\eta [q_\eta(z) f_\eta(z)] dz \quad (50)$$

$$= \nabla_\eta \int q_\eta(z) f_\eta(z) dz = \nabla_\eta \mathbb{E}_{q_\eta(z)}[f_\eta(z)], \quad (51)$$

assuming that f is well-behaved so that integration and differentiation can be interchanged.

Alternatively, the reparameterized gradient Rezende et al. (2014); Kingma and Welling (2013) can be used when there exists some distribution F not involving η and a differentiable mapping h_η such that

$$w \sim F \implies h_\eta(w) \sim q_\eta. \quad (52)$$

For example, if $q_\eta(z) = \mathcal{N}(z; 0, \eta)$ that is, a Gaussian with zero mean and variance η , one possibility is to let F be the standard Gaussian and $h_\eta(w) = w\sqrt{\eta}$.

The gradient of $\mathcal{L}(\eta)$ can be written as

$$\nabla_\eta \mathbb{E}_{q_\eta(z)}[f_\eta(z)] = \nabla_\eta \mathbb{E}_{w \sim F}[f_\eta(h_\eta(w))] = \mathbb{E}_{w \sim F}[\nabla_\eta f_\eta(h_\eta(w))], \quad (53)$$

again assuming the interchangability of integrals and derivatives. Unbiased gradients are computed as

$$g_{\text{rp}} = \nabla_\eta f_\eta(h_\eta(w)) = \nabla_z f_\eta(z) \Big|_{z=h_\eta(w)} \nabla_\eta h_\eta(w) \quad \text{for } w \sim F. \quad (54)$$

The reparameterized gradient includes gradient information $\nabla_z f_\eta(z)$ while the REINFORCE gradient does not. Taking into account the structure of f through its gradient lowers the variance of reparameterized gradient in comparison to the REINFORCE gradient. However, if z contains discrete components, there cannot be a differentiable mapping h_η , and the reparameterization trick will not apply.

B Results on a test M2 image

We evaluate StarNet on another subregion of M2. The initial 100×100 subregion of M2 considered in our main paper was located at pixel coordinates (630, 310) in SDSS run 2583, field 136, camera column 6. After fitting StarNet on this initial region x_0 , we evaluate StarNet on a neighboring region x_{test} . See Figure A.1 for locations of the considered subregions.

The subregion x_{test} has approximately 25% more stars than x_0 (1413 Hubble detections in x_{test} versus 1114 detections in x_0). Due the increased density, all methods suffered an ≈ 10 percentage point decrease in F1 score on x_{test} compared to the F1 score on x_0 (compare Table 1 and A.1).

Table A.1: Performance metrics on the M2 test subregion. StarNet-init is the network fit on the original M2 subregion (the same network as StarNet-WS in the main text). StarNet-refit ran two further wake-sleep cycles on the M2 test subregion.

Method	TPR	PPV	F1 score	#stars	(q-5%, q-95%)
DAOPHOT	0.13	0.53	0.21	338	—
PCAT	0.44	0.37	0.41	1793	(1799, 1805)
StarNet-init	0.47	0.47	0.47	1466	(1431, 1499)
StarNet-refit	0.47	0.50	0.48	1396	(1362, 1432)
Hubble	1.00	1.00	1.00	1413	—

In Table A.1 and Figure A.2, “StarNet-init” refers to the wake-sleep trained network on x_0 . Using StarNet-init and its fitted background and PSF as an initialization, we ran two

further cycles of wake-sleep on x_{test} (StarNet-refit). StarNet-refit improved the PPV over Starnet-init by two percentage points. The TPR appeared to be nearly identical across all magnitudes (Figure A.2).

These results suggest that StarNet-init extrapolates well to neighboring regions, and re-running wake-sleep is not necessary. Evaluating StarNet-init on x_{test} took 30 milliseconds. On the other hand, re-running PCAT takes another 30 minutes. Even if StarNet did require refitting, the subsequent wake-sleep cycles takes only an additional three minutes. The amortization enables StarNet inference to have much better scaling characteristics than PCAT.

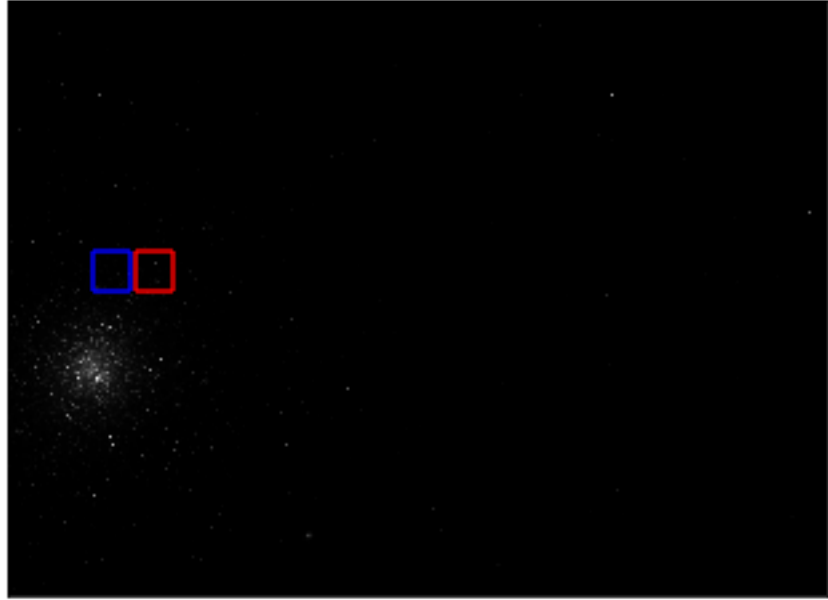


Figure A.1: The SDSS field containing M2. In red, the subregion x_0 considered in the main text. The subregion x_{test} in blue.

C Sensitivity to prior parameters

We examine the sensitivity of StarNet to prior parameters μ and α on the image M2. Recall μ is the prior mean number of stars per pixel (2); α is the power law slope on the r -band fluxes (4). In the results of Section 6, $\mu = 0.15$ and $\alpha = 0.5$.

The model appears reasonably robust. As expected, as μ increases the TPR increases while the PPV decreases – the prior encourages more detections (Figure A.3).

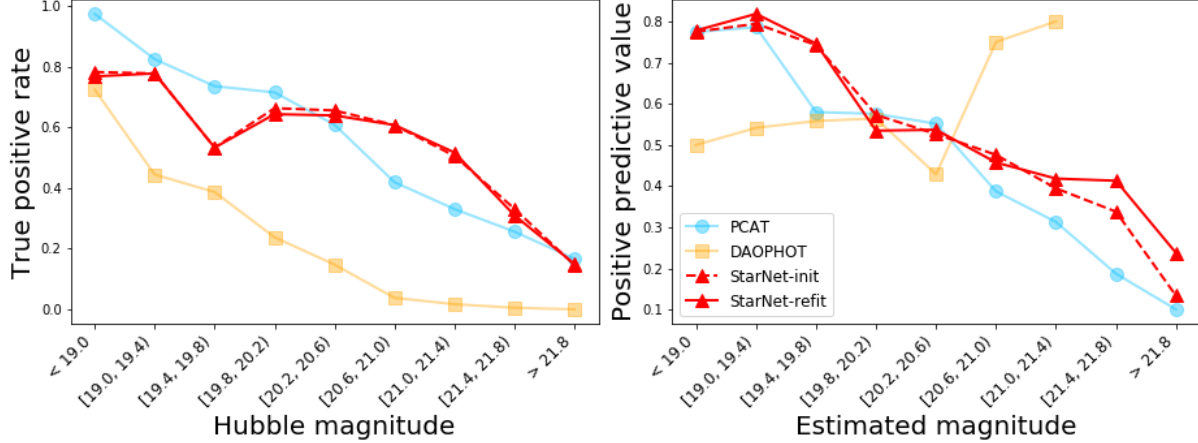


Figure A.2: True positive rate (left) and positive predicted value (right) of various methods on the M2 test subregion. StarNet-init is the network fit on the original M2 subregion (the same network as StarNet-WS in the main text). StarNet-refit ran two further wake-sleep cycles on the M2 test subregion.

As α increases, StarNet estimates more dim sources: the prior distribution on fluxes places more mass near f_{min} (Figure A.4).

While the TPR increases across α values, the PPV suffers at $\alpha = 0.75$ (Figure A.5). At $\alpha = 0.75$, we see that the TPR improves at dimmer sources at the expense of brighter sources, suggesting that the brighter sources become over-split. The stronger prior on dimmer stars also manifests in the flux distribution of the resulting StarNet catalog (Figure A.6).

D Results on Stripe-82

Most regions of the sky are much less densely populated than M2. We test StarNet on run 94, camcol 1, field 12 of SDSS, an image with light source density more typical of SDSS images. After 10 minutes of sleep training, StarNet produced a catalog on the full 1489×2048 image in ≈ 2 seconds. For comparison, the projected runtime of PCAT on an image of this size is 6 days.

Since this region of the sky is more sparse, we tile the image into 50×50 tiles; N_{max} on tiles is three. Because this region of the sky also contains galaxies, only the sleep phase was employed to fit StarNet; the wake phase would optimize the PSF to explain both stars and galaxies.

This image is contained in Stripe 82, a region of the sky repeatedly imaged by SDSS. Averaging images from different runs boosts the signal to noise ratio, resulting in a “co-added” image. We compare the performance of StarNet and PHOTO on the *non* co-added

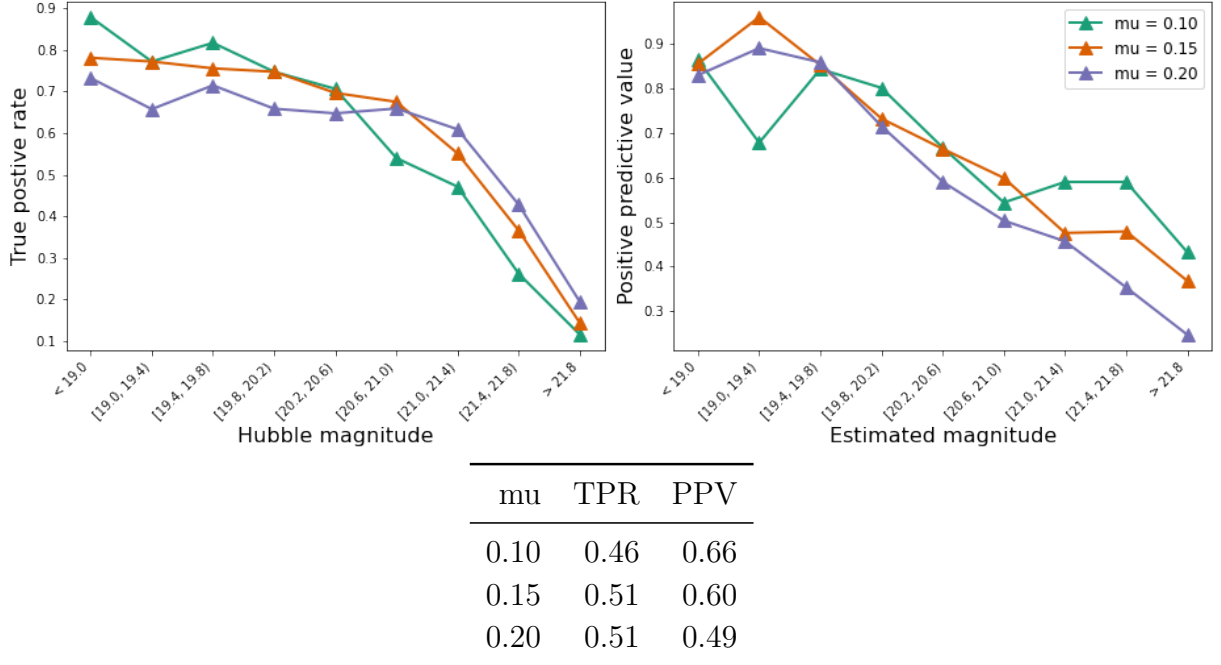


Figure A.3: Sensitivity of performance metrics to Poisson mean parameter on number of stars (μ in Equation 2).

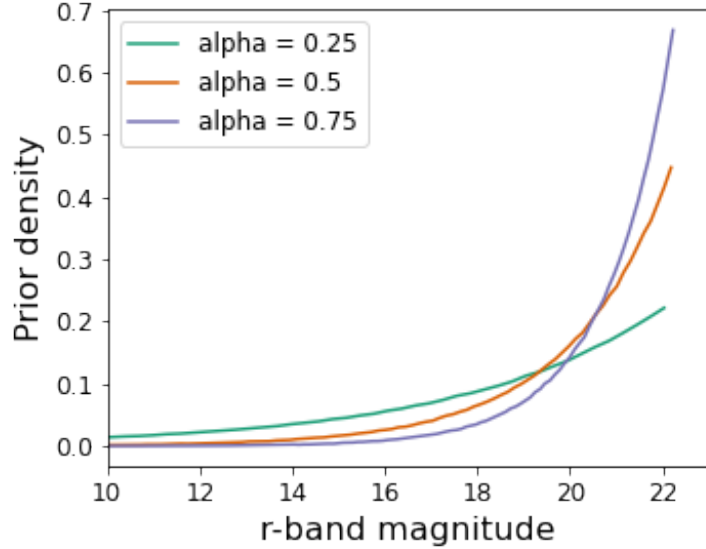


Figure A.4: The prior density of r -band magnitude for various power law slopes α .

image. The PHOTO catalog of the co-added image was used as ground truth.

The TPR of StarNet is comparable with the TPR of the PHOTO catalog on the original (non co-added) image (Figure A.7). StarNet accrues false detections, namely galaxies,

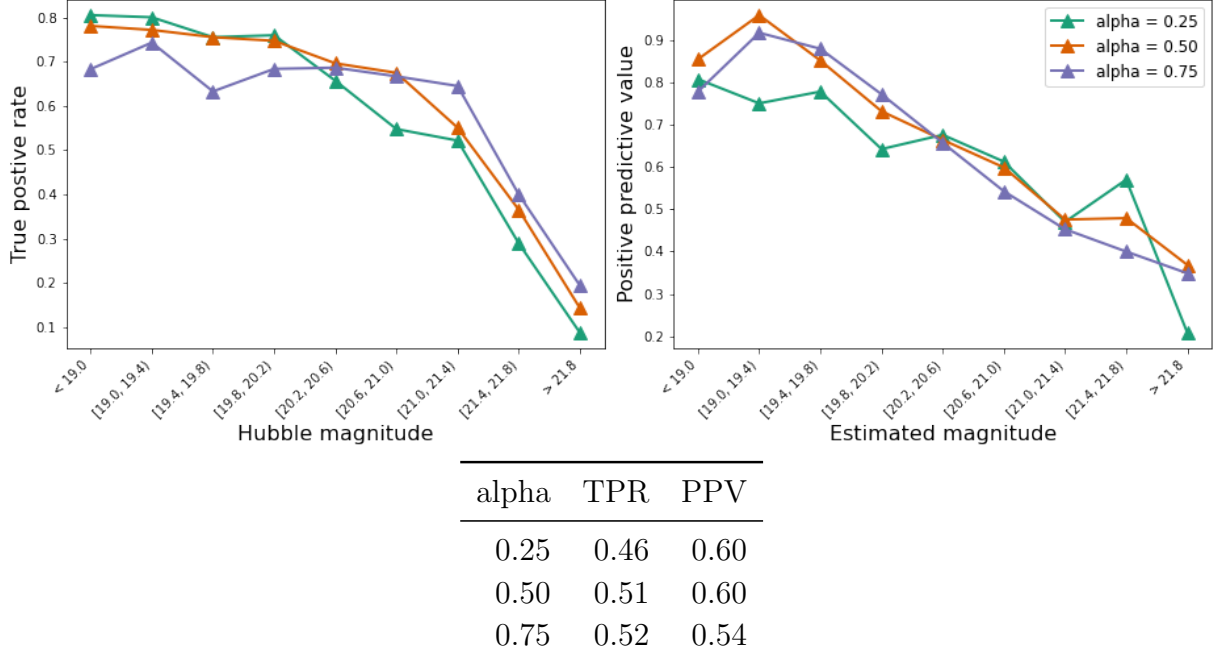


Figure A.5: Sensitivity of performance metrics to flux prior parameter α .

and thus we cannot compare the PPV. On some tiles, missed detections occur when a large galaxy within a tile causes all N_{max} detections to be placed around the galaxy – the remaining stars in the image go undetected. Incorporating a galaxy model would boost our performance.

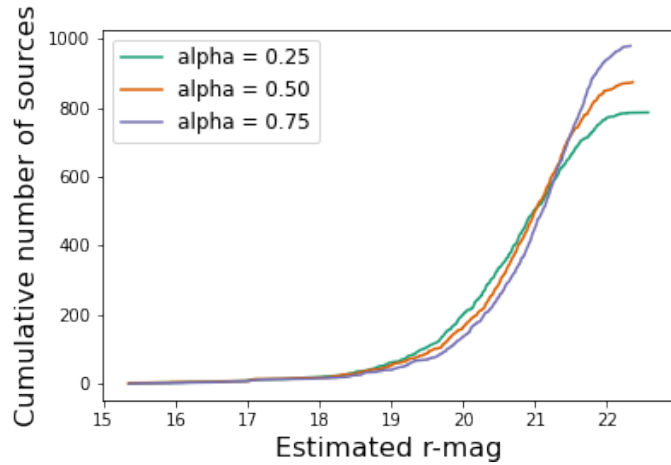


Figure A.6: Sensitivity of estimated flux distribution to flux prior parameter α .

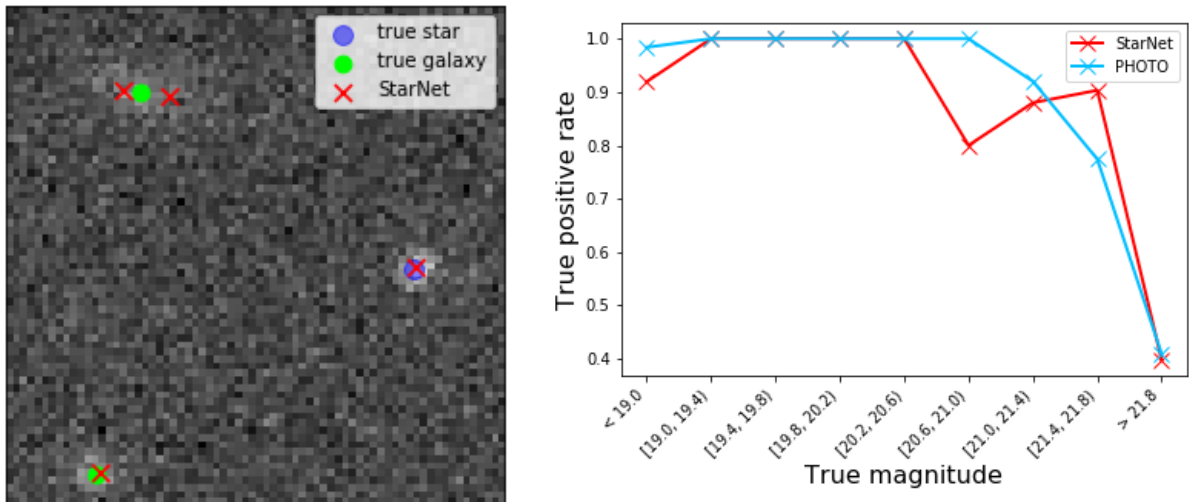


Figure A.7: (Left) Detections on a sparse field. In this example, StarNet correctly identifies the star (blue). Without a galaxy model, StarNet also classifies galaxies (green) as one or multiple stars. (Right) The true positive rate of StarNet and PHOTON as a function of true magnitude.